Universita' degli Studi di Padova

Dipartimento di Fisica e Astronomia
Galileo Galilei

Corso di Laurea in Fisica

Feasibility study of graphite-based unidirectional diagnostic calorimeter

Laureando

Lorenzo Zampieri

Relatore

Dott. Gianluigi Serianni

Co-relatore

Dott.ssa Rita S. Delogu

Anno Accademico 2014/2015

Contents

Abstract

For optimizing the neutral beam injector which will heat the nuclear fusion experiment ITER, it is necessary measuring the beam properties with a high spatial definition. For this reason, the test facility SPIDER, which is under construction in Padova, aims to realize the transport of a negative ion current similar to the one that will be used in ITER. The diagnostic calorimeter STRIKE will be employed to study the beam properties produced in SPIDER, by focusing its attention in particular on the beam uniformity and divergence. Probably, the most important pending issue in STRIKE design is how to obtain a preferential way for heat transferring into the tiles. Various solutions have been tested, including the possibility to recreate the required thermal property with an appropriate mechanical manufacturing on a graphite tile. In particular experimental conditions, an unexpected phenomenon of optical aliasing has been noticed during the LASER tests of the graphite tile prototype. The proposal of this work is to study the optical aliasing patterns occurring on the tile surface in different experimental conditions. Therefore, the attention will be focused in simulating the interaction between the thermal camera and the calorimeter. An IDL code has been developed to make possible the simulated reproduction of the patterns the thermal camera sees on the calorimeter, in all possible mutual positions of the two devices. After that, the images produced during the simulations will be compared with the real images obtained during the tests, to better comprehend the phenomenon which causes these optical aliasing patterns and to evaluate the possible consequences on STRIKE measures.

Abstract

Per ottimizzare il fascio di particelle che scalderà l'esperimento di fusione nucleare ITER, è necessario misurare i parametri del fascio ad un alta definizione spaziale. Per questa ragione mediante la test facility SPIDER, che è in costruzione a Padova, ci si propone di realizzare il trasporto di una corrente di ioni negativi simile a quella che verrà impiegata in ITER. Il calorimetro diagnostico STRIKE sarà utilizzato per studiare le proprietà del fascio prodotto da SPIDER, in particolare òa sua uniformità e divergenza. Probabilmente, la questione pendente più importante nella progettazione di STRIKE è come ottenere una direzione preferenziale per la trasmissione del calore nelle tegole del calorimetro. Sono state testate diverse soluzioni, inclusa la possibilità di ricreare la proprietà termica richiesta con un'appropriata lavorazione meccanica su una tegola di grafite. In particolari condizioni sperimentali, è stato osservato un inaspettato fenomeno di aliasing ottico durante i test di un prototipo di tegola, condotti con un laser di alta potenza. L'obiettivo di questa tesi è studiare le figure di aliasing che la termocamera fotografa sul calorimetro in tutte le possibili posizoni reciproche dei due elementi. L'attenzione verrà quindi posta nel simulare la interazione tra termocamera e calorimetro. E' stato scritto un programma in IDL che rende possibile simulare le immagini che la termocamera rivela sulla superficie del calorimetro, in tutte le reciproche posizioni dei due elementi. Dopodiché, le immagine prodotte durante le simulazioni verranno confrontate con quelle reali ottenute durante i test, con lo scopo di comprendere in maniera migliore il fenomeno che causa figure di aliasing e di valutare se questo possa portare delle conseguеze sulle misure di STRIKE.

Chapter 1

Introduction

1.1 Energetical Problem

In the last few years, the reduction of fossil fuels and the need of new energy sources are some of the most discussed themes in the scientific community. The western lifestyle, the demographic increase and the improvement of life conditions in developing countries pose the question of how could we replace, in the coming decades, the increasing needs of energy produced using fossil fuel. Moreover, the necessity of reducing the environmental pollution caused by the conventional methods of energy production is another challenge humankind must solve quickly, in order to avoid irreparable damages to the environment.

The energy production using nuclear fusion tries to give an answer to the previous questions. Nuclear fusion [1] is a reaction in which two atomic nuclei collide at very high speed and join to form a new type of atomic nuclei. If light nuclei are forced together against the electrostatic repulsion, they will fuse with a release of energy because the mass of the combination will be less than the sum of the masses of the individual nuclei. If the combined nuclear mass is less than that of iron at the peak of the binding energy curve, then the nuclear particles will be more tightly bound than they were in the lighter nuclei, and the mass decrease liberates energy according to the Einstein relationship $E = mc^2$. This nuclear reaction is due to the interplay of two opposing forces: the nuclear force which combines together protons and neutrons, and the Coulomb force which causes protons to repel each other. To reach a favorable condition which permits the nuclear fusion, it is necessary to oppose the Coulomb repulsion and bring the nuclei close enough. In this situation, the electrostatic repulsion can be overcome by the attractive nuclear force, which is stronger at close distances, and the fusion reaction is

permitted.

In the past decades, the scientific community develops two main fusion techniques in order to optimize the energy produced in this process.

- INERTIAL CONFINEMENT FUSION (ICF) is a type of fusion energy research that attempts to initiate nuclear fusion reactions by heating and compressing a fuel (mainly deuterium and tritium) target using high power lasers.
- THERMONUCLEAR CONTROLLED FUSION is a way to achieve nuclear fusion by using extremely high temperatures in a controlled environment.

This dissertation will focus its attention on the latter.

1.2 ITER Project

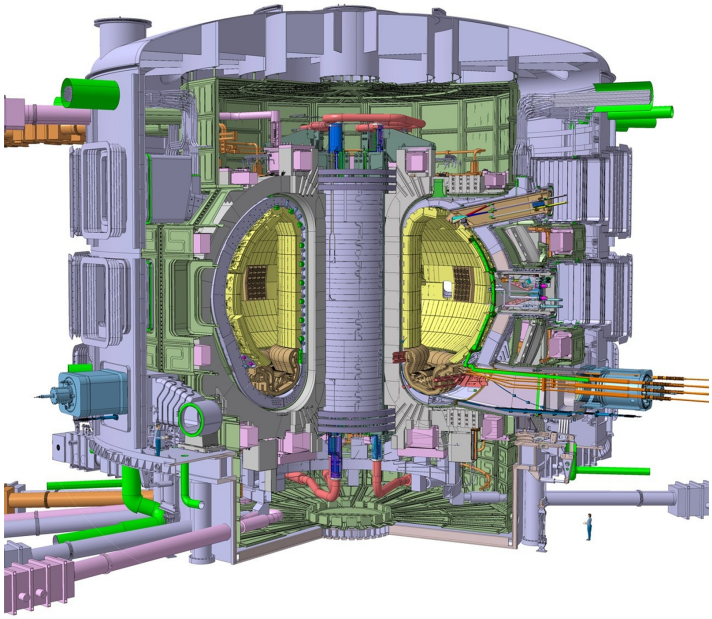

Figure 1.1: ITER reactor

ITER (International Thermonuclear Experimental Reactor) is a project funded and run by seven memberagencies: the European Union, India, Japan, People's Republic of China, Russia, South Korea and the United States. Its

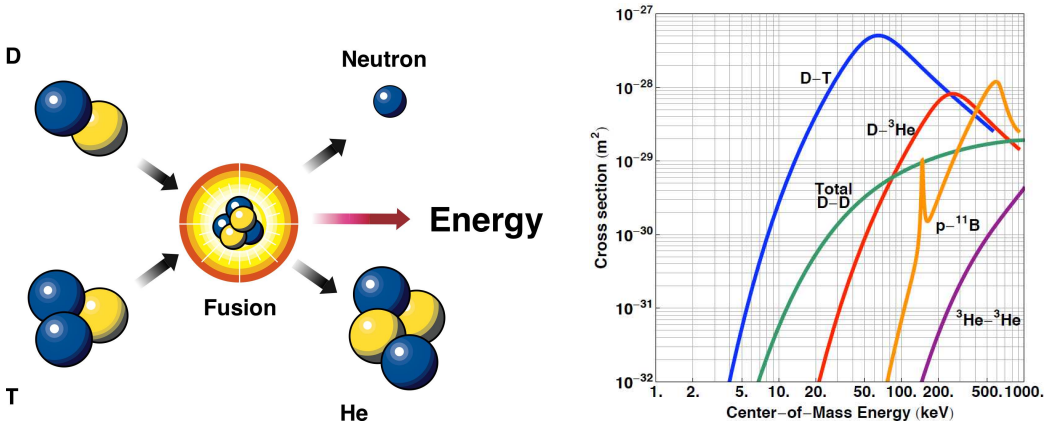

(a) Deuterium-Tritium fusion reaction (b) Cross Sections

Figure 1.2: Fusion Phenomenon and its Cross Section

proposal consists in the realization of the first prototype of a thermonuclear reactor for controlled fusion, which uses less energy than the energy it produces. To reach this target, the system confines magnetically the plasma inside the reactor at sufficient temperatures to permit the fusion reaction between deuterium and tritium nuclei. As the graph 1.2b shows, this two elements have been selected because, thanks to their small atomic number, they have the highest cross section and, at the same time, the reaction needs a lower activation energy than other elements. Consequently, it has been evaluated that this reaction also requires lower temperatures than the others, up to $20keV$. The products of deuterium-tritium fusion reactions are neutrons and ^4He atoms.

$$D + T \rightarrow^4 He(3.5MeV) + n(14.1MeV)$$

Because of their neutrality, the latter are not influenced by the magnetic fields and hit the walls of the reactor. The particle lose energy to the wall, which is made of a thermal conductor material, and this fact permits to collect energy, which can be used for producing energy for civil scope and partially for the sustainment of the reaction process. However, the presence of high energy neutrons can damage the machine and the experimental instruments. For this reason, protections in reinforced concrete have been provided in addition to protective screens to safeguard the health of men and women from radiations.

There are two different methods to furnish the sufficient energy to the plasma for starting the fusion process. The firs consists in electromagnetic radiofrequency waves sources, which heat the plasma exploiting the cyclotron

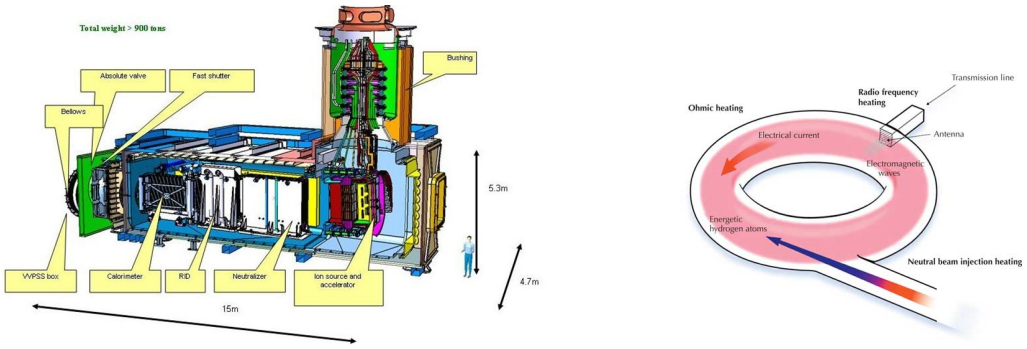

(a) NBI scheme (b) Heating systems scheme

Figure 1.3: Plasma Heater in Thermonuclear Fusion

frequency of ions (from 20 to $30MHz$) and electrons ($150GHz$). The second process is based on Neutral Beam Injector (NBI), which furnishes the kinetic energy of hydrogen or deuterium neutral gases to the plasma. ITER project involves the realization of two NBI, which will accelerate the atoms and give them an energy of $1MeV$. PRIMA project [2] (Padova Research on Injector Megavolt Accelerated), which is a prototype of the two injectors that will be used in ITER, is being built in Padova and it is the facility housing two different experimental devices.The biggest one is MITICA (Megavolt ITER Injector and Concept Advancement) which is a test facility of the same acceleration system which will be used in ITER and will give an energy of $1MeV$ to the neutral beam. The second is SPIDER (Source for the Production of Ions of Deuterium Extracted from RF plasma), which is a source of $^{-}H/^{-}D$ ions beam with an energy of $100KeV$ and a current intensity of $50A$.

1.3 The negative ion surce SPIDER

SPIDER [3] is the test facility which will study and improve the ion source properties; in particular its current, divergence and uniformity. This device is composed by three main elements. Firstly, SPIDER experiment includes the Radio Frequency Ion Source, which will have the same size as the one that will be employed in ITER neutral beam injector, and whose design is based on research and development carried out at IPP [4][5]. Inside the source, the process of negative ion productions occurs mainly with two different processes [6].

- VOLUME PROCESS: The electron binds with a hydrogen atom after the dissociation of a H_2 molecule, which was vibrationally exited after

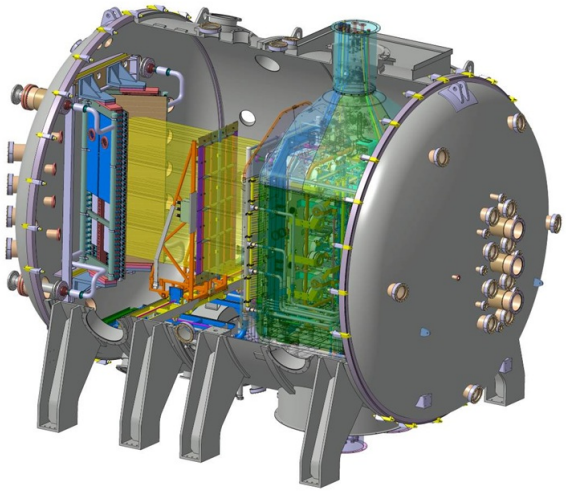

Figure 1.4: SPIDER test facility

the collision with an electron.

$$H_2^* + e \rightarrow^- H + H$$

- SURFACE PROCESS: In this case, the process is based on the conversion of hydrogen atoms which collide with the walls.

$$H, H^+ + e, 2e \rightarrow^- H$$

Secondly, extraction and acceleration system for SPIDER ion source is composed of three grids: Plasma Grid (PG), Extraction Grid (EG) and Grounded Grid (GG). Each grid features $16 \times 5 \times 16 = 1280$ apertures, where ion beamlets are extracted from ion source and accelerated up to $100kV$. All grids are made by electrodepositing pure copper onto a copper base plate, which allows complex geometrical shape and good mechanical properties. A current flowing in the vertical direction in the PG provides a horizontal magnetic field reducing the local electron density and temperature. The EG has an electric potential $9 - 10kV$ higher than the PG, to extract negative ions. Permanent magnets embedded in the EG deviate the trajectories of co-extracted electrons, forcing them to collide with the grid surface. The GG accelerates ions to 100kV and compensates for beamlet deflections in the accelerator. About 0.5MW associated to electrons exiting the accelerator is disposed of by an Electron Dump, featuring three arrays of 34 copper tubes each.

Finally, the third main element of SPIDER device is the diagnostic systems, which verify achievement of operational specifications and allow further improvements of ITER RF source. The main diagnostic system of SPIDER, which is STRIKE calorimeter, will be discussed in the following section.

1.4 STRIKE Calorimeter

STRIKE (Short-Time Retractable Instrumented Kalorimeter Experiment) is designed for investigating the beam divergence and halo and for measuring the uniformity of the ion current and of stripping losses. The beam hits directly the front side of the calorimeter and it consists of 1280 beamlets, arranged in 16 (4×4 symmetry) beamlet groups, with 5×16 beamlets in the horizontal and the vertical directions respectively in each group. STRIKE calorimeter shall provide the measurement of the heating power associated to the beam.

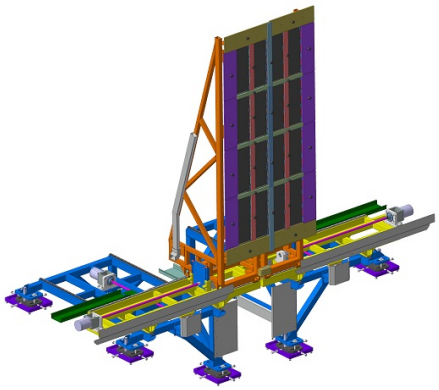

Figure 1.5: STRIKE calorimeter - Thanks to Marco Tollin.

The observation of STRIKE tiles shall be performed on the rear side because the beam particles can excite the gas between the beam source and the calorimeter, including the material sublimated from the calorimeter surfaces due to heating, thus creating an optically emitting layer; moreover debris coming off the tile surface heats up very rapidly, emitting a huge thermal radiation. In any case these radiation sources would interfere with the thermal camera if it observed the front side. Measuring the rear side temperature results in a very demanding requirement: the tile material must transfer the thermal pattern from the front to the back side without blurring it too much. The full power of beam pulse must be limited to a few seconds because of the high heat flux, which could damage STRIKE tiles. However, the duration

of the pulse must have a minimum time to let the beam source reach the steady state condition and to obtain good beam optics. For this reason, the material of the tiles shall have high melting and sublimation temperature.

Obtaining measurements in different experimental conditions shall be possible using STRIKE device. In particular, the measurement position of STRIKE can be changed so as to allow a double characterization of the beam, which results in the possibility of measuring the beam divergence and the halo. A charged particle beam is characterized by some divergence, for instance due to the repulsion force of the particles with the same charge. Halo might also be present, for instance due to the creation, in the accelerator, of neutrals which have not been fully accelerated and are no longer controlled by the electric field.

An important role in STRIKE design is played by the tile constructive materials. The main requirement is to obtain a preferential way for the transfer of heat deposited on the tile surface, from the front to the rear side of the tile. This occurs in the CFC-1D thanks to a much higher thermal conductivity in one direction than the others, obtained by arranging the carbon fibers perpendicular to the tile surface. This fiber design gives a high ratio (up to 20) between thermal conductivities along the thickness and in plane directions, but reduces the structural resistance of the material. CFC materials can resist temperatures up to $2700°C$ and temperature fluctuations of $1500°C$, which means an excellent thermal shock behavior. Another essential point is that they provide a good thermal and electrical conductivity and chemical resistance. No active cooling was adopted required because it would have interfered with the measurements by introducing thermal gradients. Indeed, it has been verified by simulation that, to cool down the tiles, thermal radiation towards the vessel is sufficient.

1.5 The infrared camera

IR thermography [7] is the main diagnostic system of STRIKE, as it measures the time evolution of the 2D temperature map at the back of the CFC tiles, from which the characteristics of the beam and of each individual beamlet can be derived, for the two operational positions of STRIKE at 500 mm and 1100 mm from the grounded grid (respectively positions A and B in Figure 1.6).

The two IR cameras shall be identical to allow easier integration and comparison of measurements. They shall cover the entire beam section and still have sufficient spatial resolution to discriminate the individual beamlets, which asks for a large number of pixels. We assume the detector has square

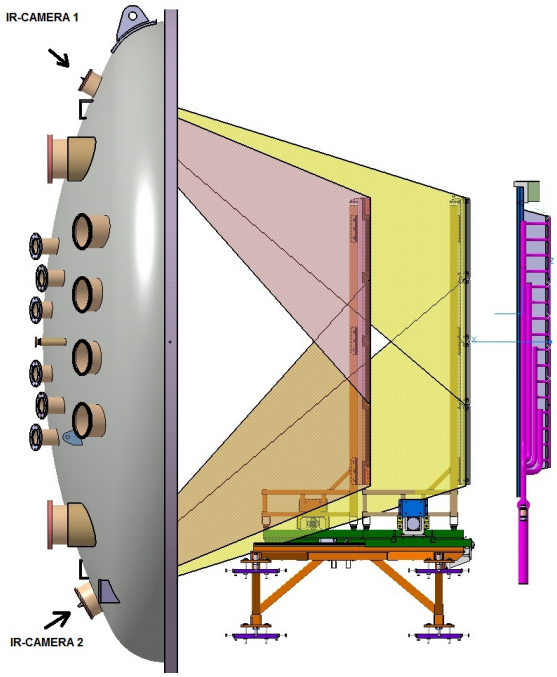

Figure 1.6: Operational position of STRIKE calorimeter

pixels and 4 : 3 format, for example 640×480 or 320×240 pixels, or not much different from it. The fixed format implies that an object $900 \times 1200 mm^2$,with STRIKE in position A, is imaged on the sensor with a resolution of 1.4-1.9 mm if 640×480, or twice it if 320×240. The variation is due to the different distances from the camera, across the observed height. When STRIKE is in position B, the spatial resolution is 25% worse, $1.8 - 2.4mm$ if 640×480, because it is further away from the camera and the same lens is used.

The simulations of the power load on STRIKE, for beam pulses up to $10s$ long, indicate that the temperature range $20 - 2000°C$ is required to be covered by the IR camera looking at the back of the tiles. Actually, for pulse repetition rates of 20 minutes the maximum temperature at the back of the tiles is expected to swing between 220 and $1700°C$ at each $10s$ pulse, already after the first pulse.

Chapter 2

Graphite option for STRIKE tiles

2.1 Alternative designs for STRIKE device

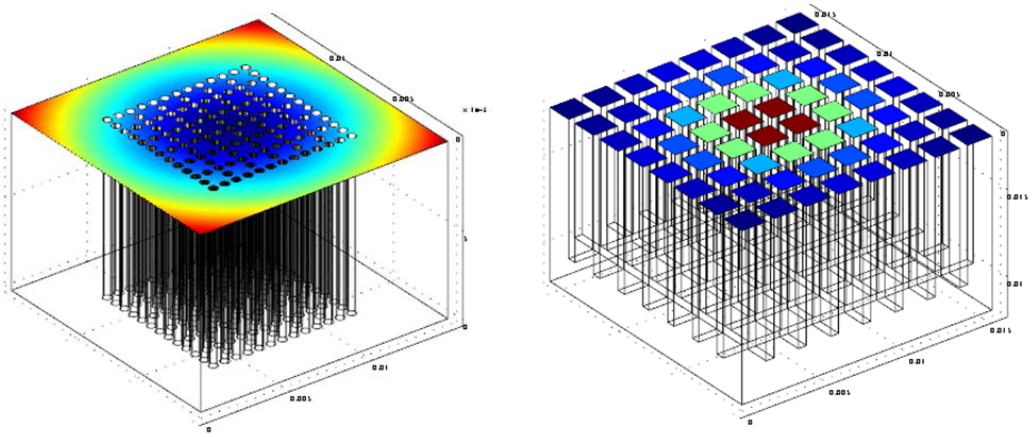

(a) drilling cylindrical holes on the graphite block

(b) prongs on the graphite block

Figure 2.1: The two different prototypes of tile

One of the most relevant pending issues in SPIDER project is the final design of STRIKE calorimeter [9]. Indeed, even if CFC-1D was indicated as the most appropriate constructive material for this device, a qualified manufacturer for this material has not been demonstrated yet. For this reason, some different alternatives are being investigated and tested, even though with possibly reduced performance of the calorimeter. An alternative material considered for the realization of our scope is simply graphite, which is an isotropic material, unlike CFC-1D. However, graphite can become isotropic

with suitable mechanical manufacturing. Two different solution, which can be appreciated in pictures 2.1, have been tested with thermal simulation:

- DRILLING CILINDRICAL THROUGH HOLES in the graphite block
- 2D ARRAY OF ELONGATED PARALLELEPIPEDS (PRONGS) is realised by machining the graphite block by digging several trenches in two directions

Some thermal simulations have been carried out for testing the different kinds of tiles, the results indicated the second one as the more promising, indeed the behavior of drilled tile is similar to the to those of a solid block of graphite, thus heat was not preferentially transferred perpendicularly to the tile surface. For this reason, this constructive approach was rejected immediately. Figure 2.2 shows the heat load after $1s$ of application in the case of castellated tile.

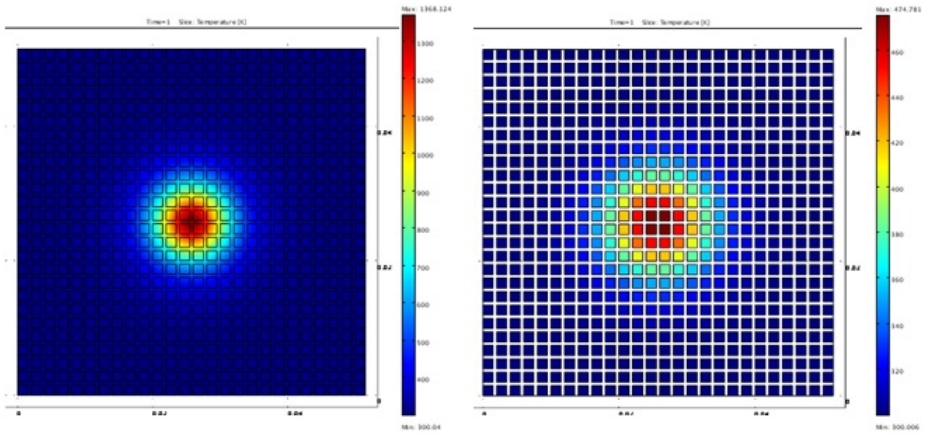

Figure 2.2: front (left hand side) and rear (right hand side) sides after 1s heat load

As can be deduced from the simulation results, the second option, which will be called "CASTELLED TILE" in the prosecution of this work, seems more interesting and applicable than the first just described. The results have been obtained by simulating a tile whose dimensions are $51.5 \times 51.5mm$ and $10mm$ of thickness, while the prong dimensions are $1.5 \times 1.5mm$, with $0.5mm$ wide trench. The heat flux applied for $1s$ is the same as one SPIDER beamlet and is expressed by the following formula.

$$\phi(x, y) = (2 \times 10^7) e^{\frac{-(x-0.02575)^2+(y-0.02575)^2}{0.005^2}}$$

As shown in Figure 2.3a, maximum temperature on the front side is about $1594K$ and maximum temperature on the rear side is about $515K$, after $1s$ of heat load application. The Figure 2.3b lists the effects of successive beam pulses, with a starting temperature 600K. Maximum temperature on the front side is about $2000K$, while maximum temperature on the rear side is about $744K$ after $1s$ heat load application.

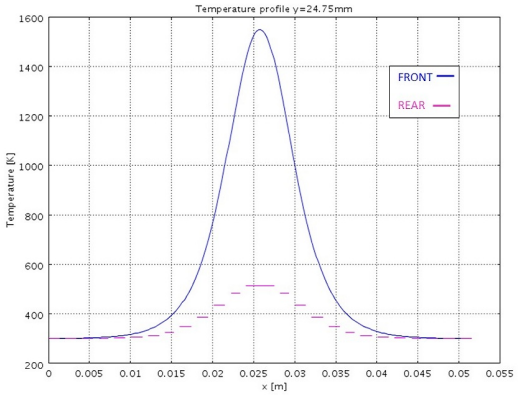

(a) Front and rear side temperature, 300K uniform starting temperature

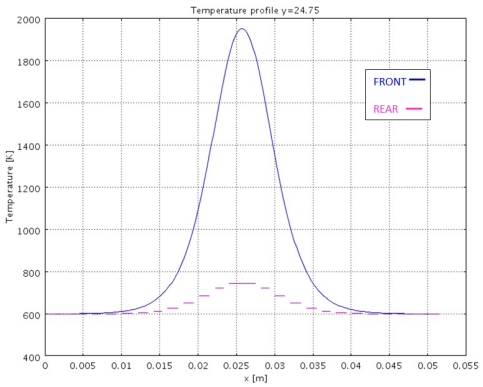

(b) Front and rear side temperature, 600K uniform starting temperature

Figure 2.3: Simulations in different conditions

Figure 2.4: Thickness of tile solid part

The thickness of the solid part of the tile, which is indicated in Figure 2.4, is fixed to a value of $2mm$. In this way, two different contributes of this element are balanced with the best compromise. On one hand, the solid part should be thick since it to absorb heat and consequently to maintain the front temperature lower, on the other hand it cannot be too thick, because otherwise the thermal front covers a higher distance before reaching the prongs, so the footprint of the beam broadens and the pattern at the rear side is more distorted.

2.2 LASER tests on castellated tile

Based on the simulation, two prong tiles made of graphite were manufactured. Their dimensions are $47.5 \times 47.5mm$ for the first, which has been realized by electroerosion, and $119.5 \times 89.5mm$ for the second, realized by mechanical machining. Prong dimensions are in both of cases $2.5mm$ of square side, $0.5mm$ trench and $8mm$ depth, for a total thickness of the tiles of $10mm$. These samples (the biggest is shown in picture 2.5a) were tested with a power laser in different experimental conditions. The next sections will report the test results.

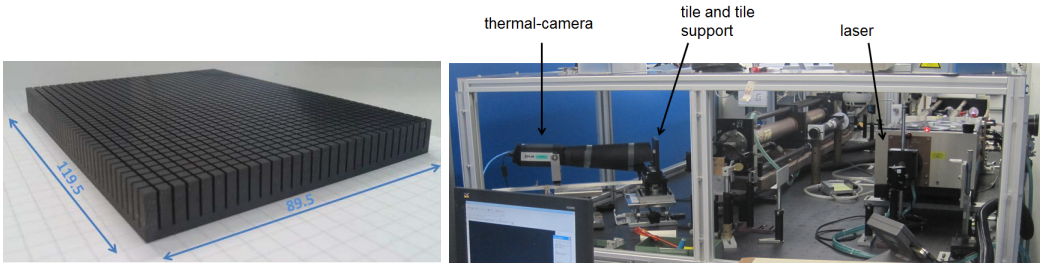

(a) Prong tile realised by mechanical machining

(b) Experimental bench

Figure 2.5: Experimental devices

Firstly, a test done using the square tile ($47.5 \times 47.5mm$) is reported. The distance between thermal camera and tile is $0.3m$ and the observation angle of the infrared-camera, with respect to the normal to the tile, is $0°$. Heat load duration is $5s$ with a power of $60W$. In Figure 2.7 the maximum temperature trend has been reported, an increase between 1s and 6s can ben noticed. Therefore, the maximum temperature value on the rear side is reached $1s$ after the end of the heat load application. At the end of the laser pulse, tile temperature obviously decreases and in the tail of the curve, a thermalisation of the device occurs. The highest temperature value is found at the point indicated in Figure 2.6, during the load application. 2.6

Secondly, another test done using the same square tile is reported. In this test, the previous spatial parameters have been mantained but the heat load application have been protracted to $20s$. The maximum temperature value on the rear side is reached $1s$ after the end of the heat load application, as shown in picture 2.8. In any case, the temperature delay between front and rear side increases for higher temperatures.

Another important element to underline is the reflectivity of the tile. This was measured by exposing the solid side of the graphite sample to the power

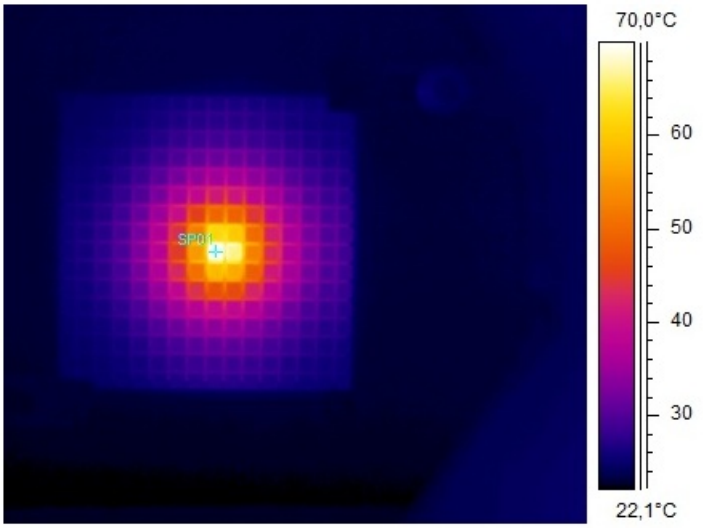

Figure 2.6: Thermal camera image of the rear side

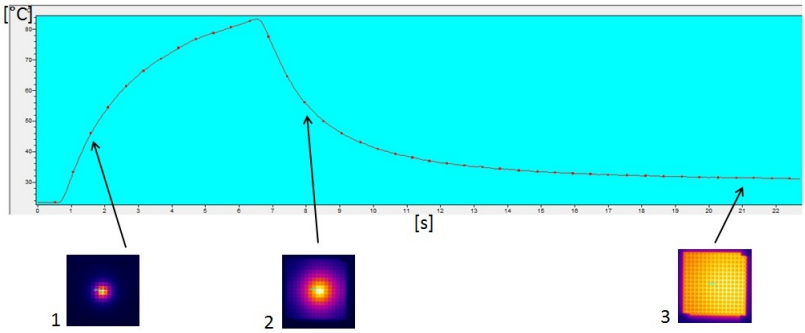

Figure 2.7: Maximum temperature trend on the rear side (4s pulse)

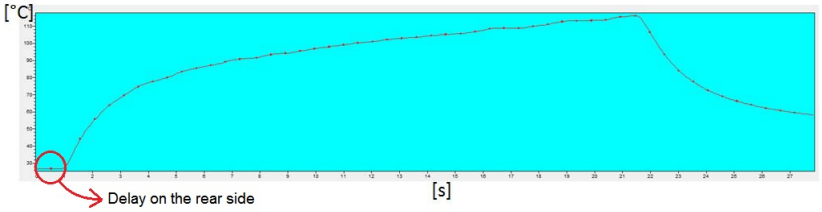

Figure 2.8: Maximum temperature trend on the rear side (20s pulse)

laser and by measuring the reflected radiation. The results show that 35% of radiation is reflected, while only 65% increases the tile temperature. It can be noticed that the reflectivity is quite high compared to CFC-1D; for this reason the tile surface have to be rough, in order to increase the emissivity. Secondly, faster heat transfer can be noticed from the front to the rear side of the heat front in CFC than in graphite. Therefore graphite calorimeter will not have the same efficiency in transfering heat as CFC-1D tiles; in particular this will result in higher temperature on the front side

2.3 Evidences of aliasing phenomenon

The aliasing, is maybe the most unexpected drawback noticed during the tests. The infrared camera, as well, reveals particular patterns on the rear side of the tile in special experimental condition. An example of the latter can be viewed in the Figure 2.9; this kind of optical aliasing phenomenon is known as Moirè effect. These patterns occur when the thermal camera is far away from the tile, about 2.9-3.5m, which will be the operating distances in SPIDER during normal experimental conditions. As can be noted from Figure 2.9, the patterns do not correspond to the original ones (Figure 2.6). In particular, the distance between light and deep band is completely different from the real spacing of tile trench.

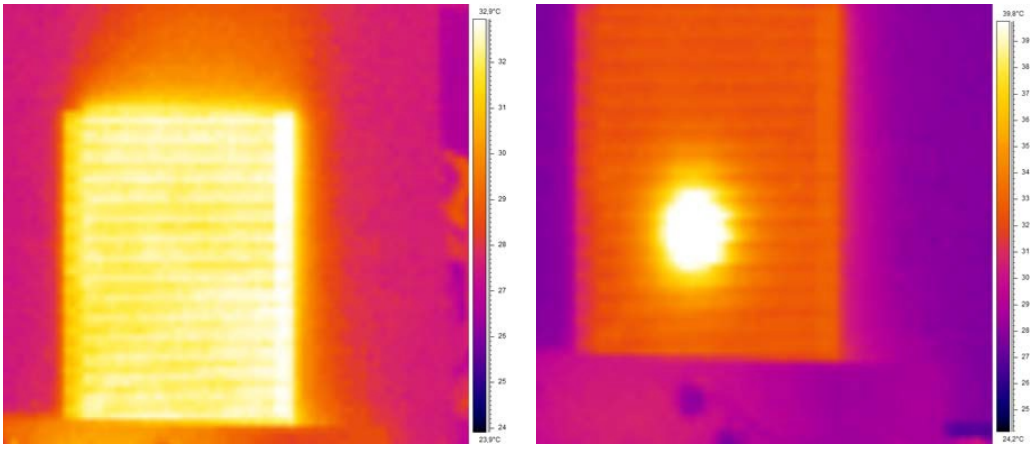

(a) Before the pulse (b) During the pulse

Figure 2.9: Moiré effects - distance $2.9m$

The previous images represent the tile before the pulse and the tile during the pulse. In first two pictures (Figure 2.9), the distance between infrared

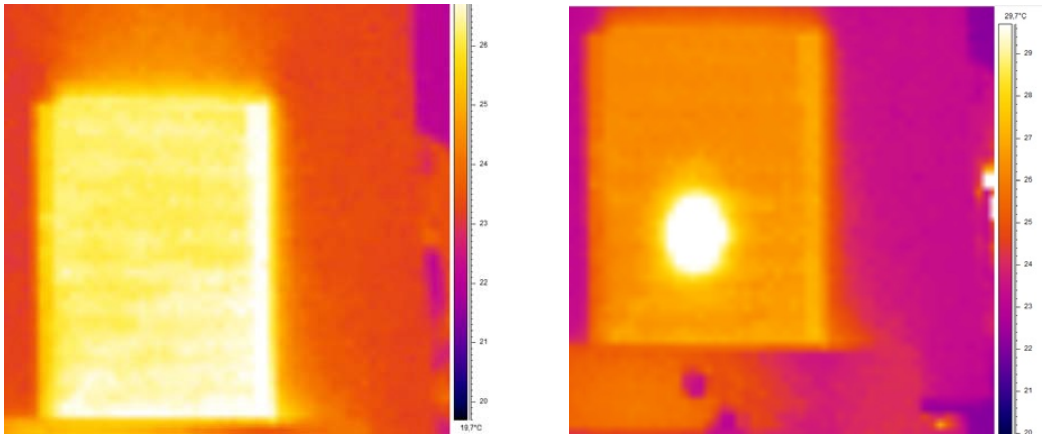

(a) Before the pulse (b) During the pulse

Figure 2.10: Moiré effect - distance $3.38m$

camera and tile is $2.9m$ while in the second two(Figure 2.10), the distance between the two elements is $3.38m$. The observation angle of the infrared camera, with respect to the normal of the tile, is $\theta = 55°$ for both the distances.

The main elements of moirè effect theory will be treated in the following chapter.

Chapter 3

Theory of moiré effect

3.1 Basic elements

The moiré effect [12] is a well known phenomenon which occurs when repetitive structures (such as screens, grids or gratings) are superposed or viewed against each other. It consists of a new pattern of alternating dark and bright areas which is clearly observed at the overlapping, although it does not appear in any of the original structures. Moiré phenomen has found a vast number of applications in many different fields. For example in strain analysis moirés are used for the detection of slight deflections or object deformations, and in metroloy moirés are used in the measurement of very small angles or movement. Moiré patterns are commonly seen on television screens when a person is wearing a shirt or jacket of a particular weave or pattern, such as a houndstooth jacket and photographs of a TV screen taken with a digital camera often exhibit this particoular patterns as well. To give an example, in Figure 3.1 a strong moiré pattern can be seen. These patterns are created by the superposition of the plumage of a parrot, which can be considered as a sort of grating system.

Several matematical approaches can be used to explore the moiré phenomenon [12]. *The classical geometric approach* is based on a geometric study of the properties of superposed layers, their periods and their angles. By considering relations between the superposed layers, this method leads to formulas that can predict, under certain limitations, the geometric properties of the moiré patterns. Another approach in use is *the equations method*, which is a pure algebric approach, based on the equations of each family of lines in the superposition. This approach provide the same results as the previous method. The most complete approach to examine this phenomenon based on the superposition of periodic structures is *the spectral approach*, which ex-

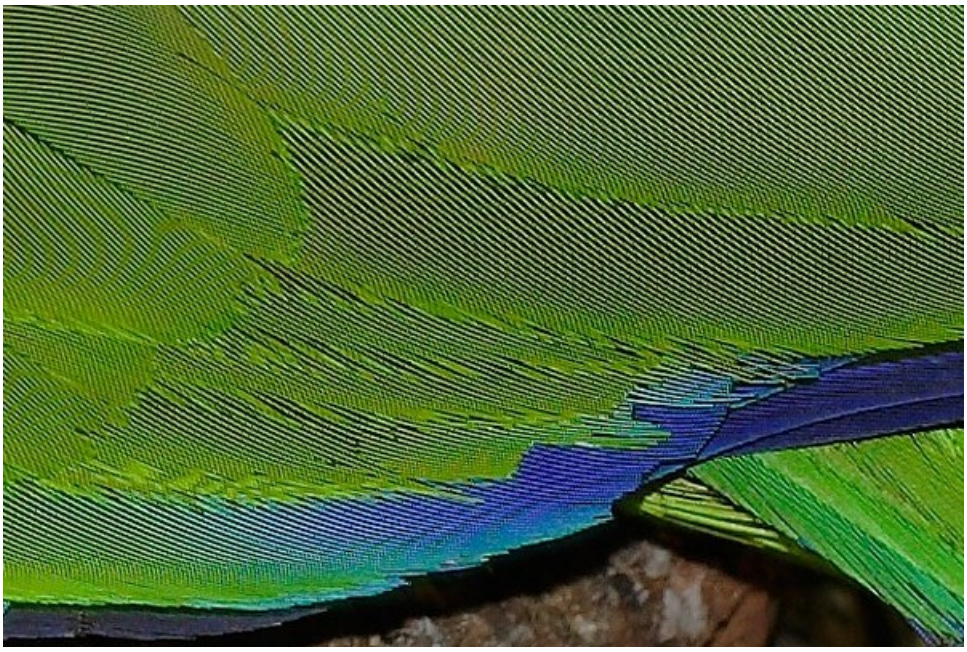

Figure 3.1: Strong moiré patterns visible in this photo of a parrot feathers.

ploits the Furier theory. Unlike the previous methods, this approach enables to analyze propeties not only in the original layers and in their superposition but also in their spectral rapresentation, therefore this offers a more profound understending of the problem.

In the following paragraphs, some basilar examples of moiré phenomena will be explained using the geometrical approach mainly. These theoretical examples will reproduce the results of the simulations, reported in chapters 6 and 7.

3.2 Moiré effec for parallel patterns

Let us consider two patterns made of parallel and equidistant lines, for example vertical lines, as shown in Figure 3.2. The step of the first pattern is p, the step of the second is $p + \delta p$, with $0 < \delta < 1$. If the lines of the patterns are overlapped at the left of the figure, the shift between the lines increase when going to the right. After a given number of lines, the patterns are opposed: the lines of the second pattern are between the lines of the first pattern. If the picture is looked from a far distance, the observer has the feeling of pale zones when the lines are superimposed (there is white between the lines) and of dark zones when the lines are "opposed".

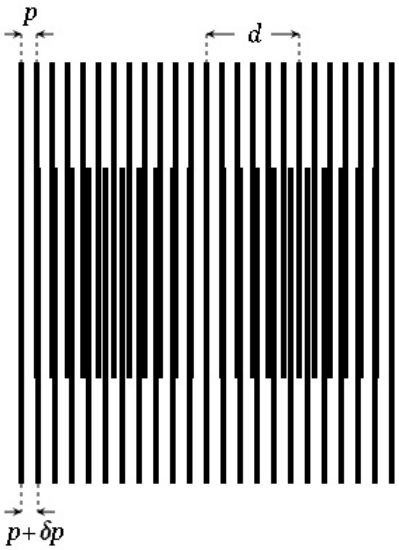

Figure 3.2: Parallel and equidistant lines.

When the shift between the two is equal to $\frac{p}{2}$, there is the first dark zone. The n^{th} line of the second pattern is shifted by $n \cdot \delta p$ compared to the n^{th} line of the first network. The middle of the first dark zone thus corresponds to

$$n \cdot \delta p = \frac{p}{2}$$

and extracting n

$$n = \frac{p}{2\delta p}$$

The distance d between the middle of a pale zone and a dark zone is

$$d = n \cdot p = \frac{p^2}{2\delta p}$$

the distance between the middle of two dark zones, which is also the distance between two pale zones, is the double of the previous quantity

$$2d = \frac{p^2}{\delta p}$$

From this result we can deduce two main pieces of information. First of all, the bigger the step, the bigger the distance between the pale and dark zones and then the bigger the discrepancy δp, the closer the dark and pale zones; a large spacing between dark and pale zones mean that the patterns have very close steps. An extreme situation is, of course, when $\delta p = \frac{p}{2}$. In this case the result is a uniformly grey figure, with no contrast.

3.3 Rotated patterns

As a second example, let us consider two patterns with the same step p, but the second pattern is rotated by an angle α with respect to the first. As shown in picture 3.3, seen from afar, dark and pale lines can be seen as well: the pale lines correspond to the lines of nodes, that is, lines passing through the intersections of the two patterns. This is a common situation which is typical in our everyday life.

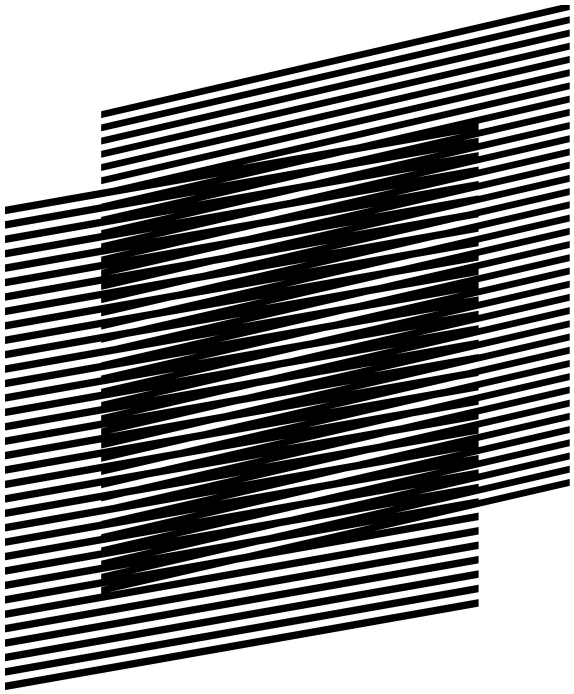

Figure 3.3: Rotated patterns.

In the scheme of picture 3.4, the enlargement of a grid pattern cell is reported. It can be seen that the shaped geometric figure is a parallelogram, and in this particular situation, where $p' = p''$, it is a rhombus. Using the trigonometrical relations, it is easy to see that

$$d = \frac{p}{\sin \alpha}$$

Let us call D the half of the larger diagonal. Moreover, D is the spacing between two pale lines.

$$(2D)^2 = d^2(1 + \cos \alpha)^2 + p^2$$

$$(2D)^2 = \frac{p^2}{\sin\alpha^2}(1+\cos\alpha)^2 + p^2$$

$$(2D)^2 = p^2\left(\frac{(1+\cos\alpha)^2}{\sin\alpha^2} + 1\right) = 2p^2\left(\frac{1+\cos\alpha}{\sin\alpha^2}\right)$$

Using the bisection relation $\left|\sin\left(\frac{x}{2}\right)\right| = \sqrt{\left(\frac{1-\cos(x)}{2}\right)}$, the following expression can be deduced with some simple calculus.

$$D = \frac{p}{2\sin\frac{\alpha}{2}}$$

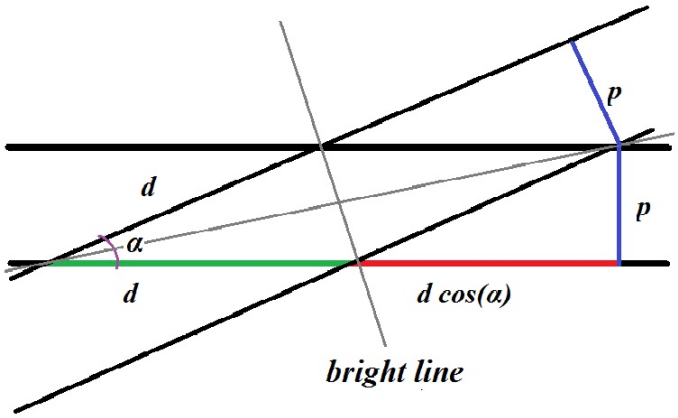

Figure 3.4: Cell scheme.

If α is small, at least $\alpha < \frac{\pi}{6}$, then $\sin\alpha \approx \alpha$ and

$$D \approx \frac{p}{\alpha}$$

$$\alpha \approx \frac{p}{D}$$

We can see that the smaller the α, the farther the pale lines; when the patterns are parallel ($\alpha = 0$), the spacing between the pale lines is "infinite" (there are no pale lines). Similar dependencies can be obtained if we consider $p' \neq p''$, however the formalization requires a different analytical approach.

3.4 Complex and curved patterns

Obviously, more complex moiré patterns [13] can be obtained by the overlapping of more than two periodic grids or by the superposition of curved lines.

In the next pictures, some typical examples are reported in order to give a better and more complete comprehension of this phenomena but without the claim of a complete mathematical formalization, which is out of the scope of the present work.

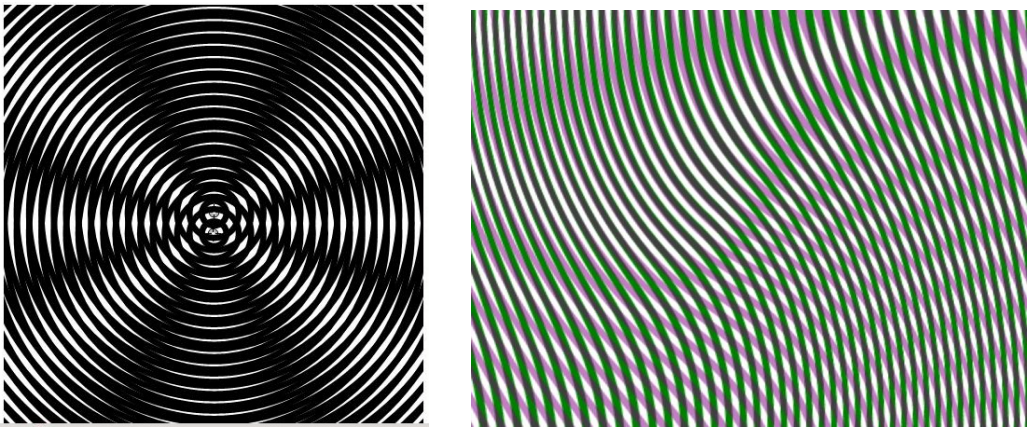

(a) Circles superposition. (b) Curve lines superposition.

Figure 3.5

Chapter 4

The simulation program

4.1 The fundamental idea

To have a better comprehension of moiré patterns which occurs on the tile surface, an IDL code [14] has been written. This code tries to reproduce the interaction between the infrared camera and the tile. The main idea rises from the experimental observation that moiré patterns occur when the pixel of the camera has a comparable dimension with respect to the lattice of the calorimeter.

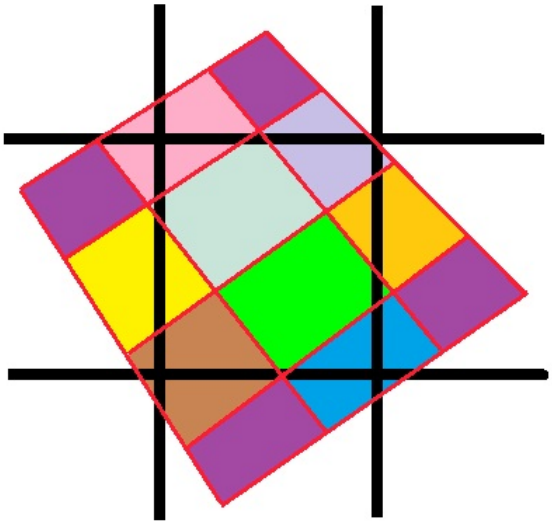

Figure 4.1: Pixel intersects the prongs.

To give an example, a pixel (the central square black bordered), which intersects various prong whith different colours (corresponding to different

temperature) is reported in Figure 4.1.The final temperature of a pixel, according to Moirè effect, will be then affected by the contributions of its neighbours.

4.2 The algorithm

The code has been customized to manage both artificial and real images. In the first case, the program works producing a virtual tile with assigned temperatures, while in the second case it gets the temperature from a real image. The main steps of the code can be summarized as follows:

- DEFINITION OF GRIDS PROPERTIES: The first step defines the grid. The sensor of the camera is considered as an orthogonal fixed grid, called T-grid (Figure 4.2). The calorimeter grid, C-grid, is defined by free parameters (amplitude and orientation of the grid). The parameters of C-grid are extablished by the perspective laws, both for what concerns the distance between the two experimental devices and the angle of observation. Each cell is associated to a number representing the temperature of the cell itself, now expressed in an arbitrary measurement unit. The grids have been defined in a cartesian coordinate system (x, y), the vertical straight lines are parameterized as $x(y)$ while the horizontal straight lines as $y(x)$. In this way, the degeneration of the slope can be easily removed and never reaches infinite. The intersection points of the grids are saved in array. The points are parameterized using their cartesian coordinates (x_i, y_i).

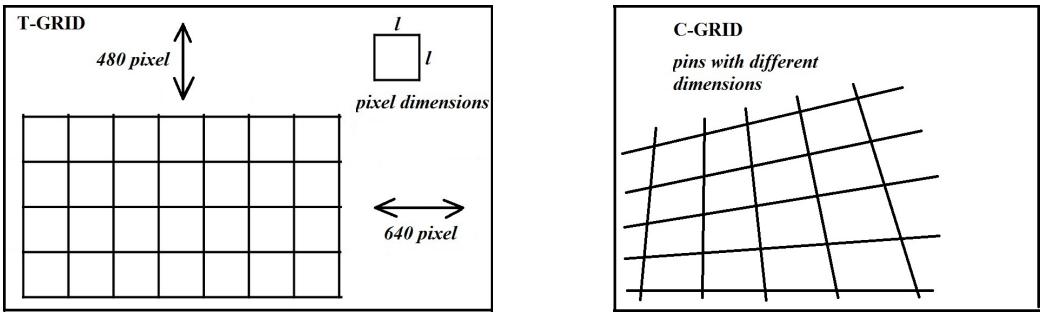

(a) T-grid (b) C-grid

Figure 4.2: The grids used in simulations.

- A "MAXIMAL GRID" IS DEFINED FOR EACH CELL OF THE T-GRID: To give an example, in figure 4.1 the maximal grid of the central

T-cell is outlined in red and consists in the set of calorimeter colourful cells, which cover the whole T-cell.

- FOR EACH CELL OF MAXIMAL GRID WE CALCULATE THE OVERLAP AREA: The intersection of T-grid and C-grid cells produces irregular polygons. The overlap area is the polygon resulting from of the intersection of a T-grid cell and each element of the maximal grid. That area can coincide with the whole area of the maximal grid element, if the C-grid cell belonging to the maximal grid is totally included into a T-grid cell (red area in Figure 4.3) or can result in a partial interception (blue area). The area of each polygon is evaluated by the Shoelace Algorithm.

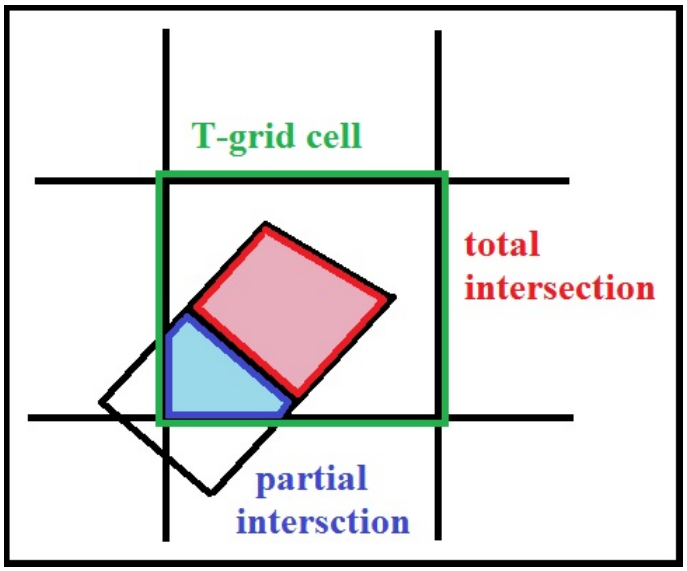

Figure 4.3: Possible intersection cases.

- WEIGHED AVERAGE: The weighed average of the temperature on each T-grid cell is calculated, the weight is simply the overlap area evaluated in the previous step.

To conclude this section in Figure 4.4, the main flow chart summarizes the algorithm.

The second flowchart, Figure 4.5, explains the function which evaluates the maximal grid of a single T-gid cell.

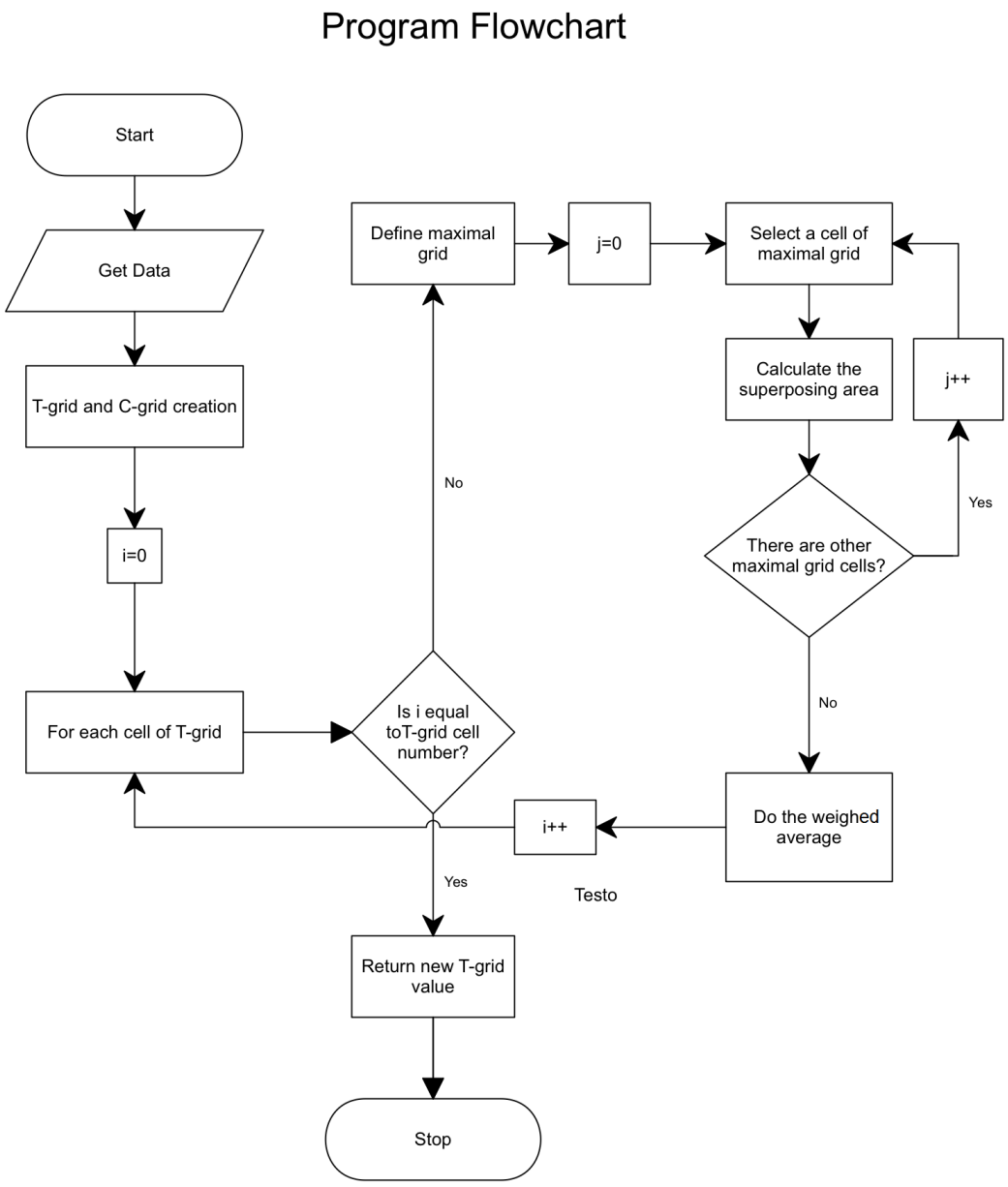

Figure 4.4: Main program flowchart.

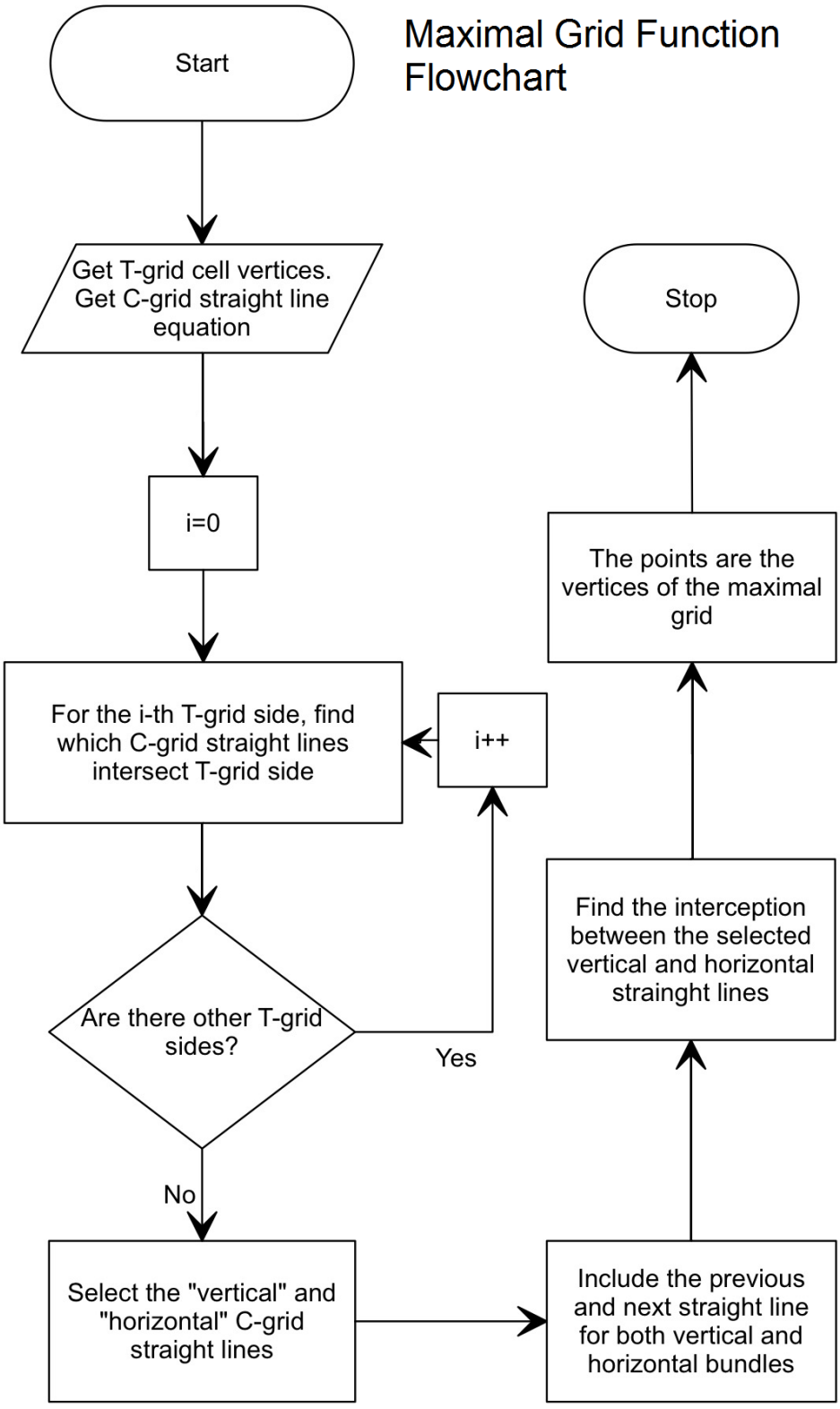

Figure 4.5: Maximal grid function flowchart.

4.3 Image processing examples

In the following paragraph, two simple examples are discussed to better explain the code and its results. IDL environment recognises the colours of pictures and associates a number to each colour. This number is included in the interval $[0; 255]$, where 0 corresponds to black and 255 to white. The other colours correspond to intermediate elements of the interval; obviously the darkest colours are close to 0 while thelightest colours to 255. After that, the picture is converted into a bidimensional array which has the same dimensions as the image resolution. The image resolution is thus modified in relation to T-grid size.

For the first example, Figure 4.6 has been used as original image.

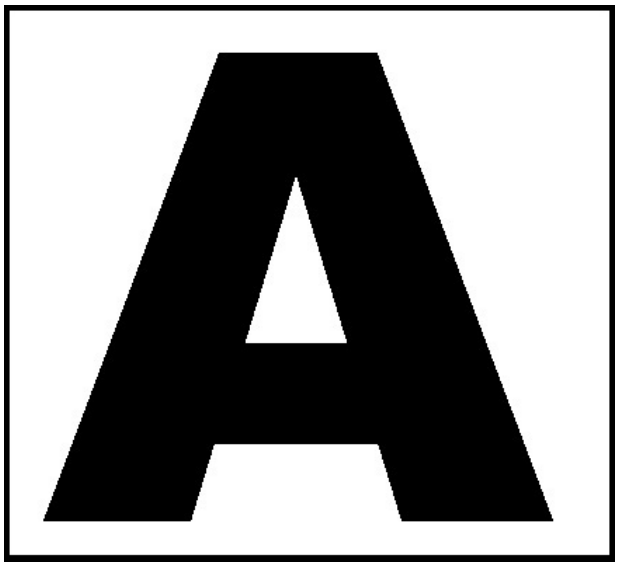

Figure 4.6: Example 1 - Original image.

In the first example, the resolution of the original image "A", which becomes our C-grid, is $435 \times 397 pixels$. Every pixel of the image is thus a cell of the C-grid; these pixels are very small with respect to the dimensions of the letter A, which is thus well resolute. The side of T-grid cell is equal to 15 pixel of the original image, as can be noted in Figure **??**, where T-grid is represented in green colour. Since T-grid cell is bigger than the pixel of the original image (C-grid), T-cells will certainly intersect more than one pixel. In this example, two tipical situations can thus occur. The first possibility is that all pixels intersected are monocromatic; in this case the colour of T-grid cell will be the same as the original pixels. The second possibility is that T-grid cell intersects both black and white pixels; in this case the final colour

will be the weighed average of the two starting colours. The result is shown in Figure 4.7, where a part of T-grid is underlined in green.

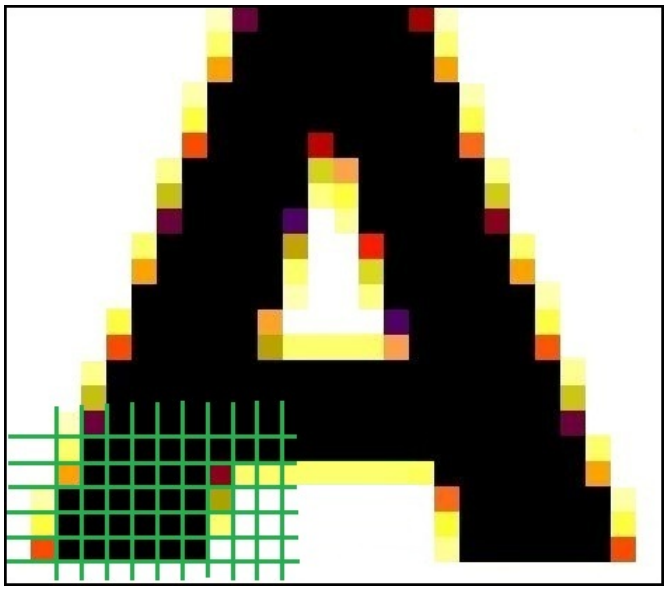

Figure 4.7: Example 1 - Processed picture.

Another example is reported to better understeand the operation of the program. Figure 4.8 is the image of our C-grid. It consists simply in a sequence of monospaced black and white lines. In the resulting images (Figure 4.9a and 4.9b), two differnet moiré patterns appear.

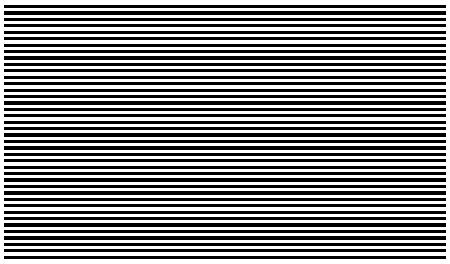

Figure 4.8: Example 2 - Original line sequence.

In Figure 4.9a, the T-grid superposed has a side step slightly bigger than the one of original image. A moiré pattern can be noted and it is ascribable to the pattern described in section 3.2 . In Figure 4.9b, a rotated T-grid has been superposed with respect to the original image and a moiré pattern can be noted also in this situation. However, the theoretical model which explains this pattern is the teory of moiré produced by rotated parallel pattern, described in section 3.3.

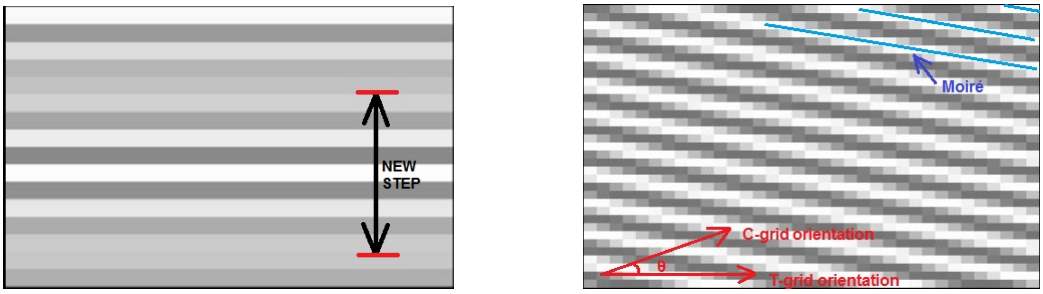

(a) Parallel pattern (b) Rotated pattern

Figure 4.9: Two moiré examples obtained with program elaboration.

4.4 Thermal camera correct vision

To have a physical relevance of the moiré effect for SPIDER calorimeter, it is appropriate to better comprehend the phenomenon which allows the infrared camera operation.

4.4.1 From Temperature to Emissive Power

As shown in Figure 4.10, infrared energy is just one part of the electromagnetic spectrum, which encompasses radiation from gamma rays, x-rays, ultra violet, a thin region of visible light, infrared, terahertz waves, microwaves, and radio waves. These are all related and differentiated in their wavelength or frequency. All objects emit a certain amount of black body radiation as a function of their temperatures. Generally speaking, the higher an object temperature, the more infrared radiation is emitted as black-body radiation. The camera sensor collects this radiation, which is converted into an electronic signal and transformed into images displayed in pseudo-color, where changes in color are used rather than changes in intensity to display changes in the signal. Our thermal camera [11] uses a microbolometer, which is an uncooled thermal sensor. Infrared radiation with wavelengths between $7.8\mu m - 14\mu m$ strikes the detector material, heating it, and thus changing its electrical resistance. This change is measured and processed into temperatures which can be used to create an image.

For this reason, it has been understeand that the quantity measured by the sensor is not the temperature, but it is the energy flux which heats the microbolometer surface, while temperature is calculated undirectly with an analytic calibration. This is an important result because it means that moiré patterns are not caused by the different temperatures of the prong, but by the different energy fluxes the prongs emit. Thus, T-grid have to record

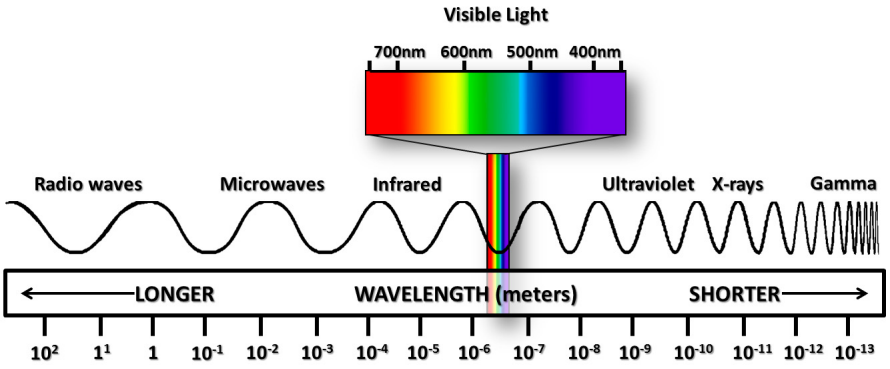

Figure 4.10: Electromegnetic spectrum.

the energy fluxes emitted from the C-grid, instead of the temperatures of its prong. The expression of energy flux is well known from Planck's black body theory [14], developed at the beginning of the 20^{th} century, and it is expressed by Stefan–Boltzmann law. Different planckian curves for various temperatures are reported in figure 4.11. Specifically, this law states that the total energy radiated per unit surface area of a black body across all wavelengths per unit time (also known as the black-body radiant exitance or emissive power), J, is directly proportional to the fourth power of the black body thermodynamic temperature T, as shown in the following steps.

$$J = \int_0^\infty I(\nu)\, d\nu = \int_0^\infty I(\lambda)\, d\lambda$$

The expressions of $I(\nu)$ and $I(\lambda)$ are well known but we report only $I(\lambda)$ because we will use λ as variable in our dissertation.

$$I(T) = \frac{2\pi hc^2}{\lambda^5} \frac{1}{e^{\frac{hc}{\lambda kT}} - 1}$$

The result of the integration is

$$J = \int_0^\infty I(T) d\lambda = \int_0^\infty \frac{2\pi hc^2}{\lambda^5} \frac{1}{e^{\frac{hc}{\lambda k_B T}} - 1} d\lambda = \frac{2\pi^5 k^4}{15c^2h^3} T^4 = \frac{\pi^2 k^4}{60\hbar^3 c^2} T^4$$

Using the expression σ for the Stefan-Boltzman constant

$$\sigma = \frac{2\pi^5 k_{\mathrm{B}}^4}{15h^3c^2} = \frac{\pi^2 k_{\mathrm{B}}^4}{60\hbar^3 c^2} = 5.670373(21) \cdot 10^{-8}\ \mathrm{J\,m^{-2}\,s^{-1}\,K^{-4}}$$

We obtain the final result

$$J = \sigma T^4$$

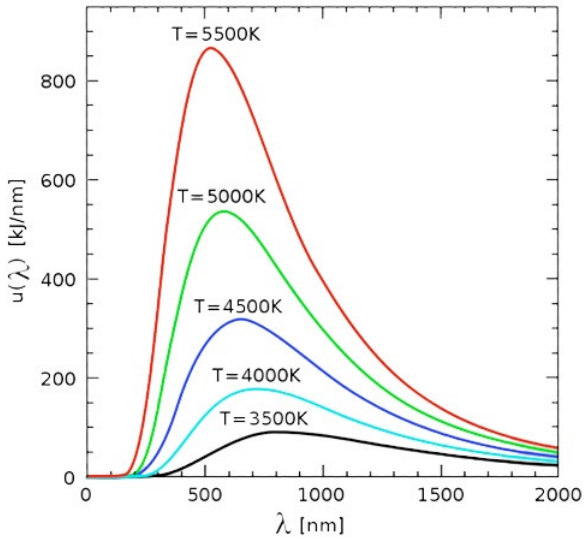

Figure 4.11: Planckian curve at various temperatures.

However, the sensor of the camera is obviously not sensible to all the electromagnetic spectra but, as said before, it detects a wavelength range between $7.8\mu m - 14\mu m$. In this context, the integration extremes $[0, \infty]$ lose their meaning and consequently, the Stefan-Boltzmann law is no more valid. To obtain a correct value of J, the thermal camera wavelenght range have to be the integration extremes. The integral has no analytical solution and must be calculated using the function $\mathrm{INT}_T ABULATEDofIDL.J = \int_{7.8\mu m}^{14\mu m} \frac{2\pi hc^2}{\lambda^5} \frac{1}{e^{\frac{hc}{\lambda k_B T}} - 1} d\lambda$

4.4.2 Temperature calibration

The the program evaluates the contribution of the different emissive power of each pixel. However, the thermal camera gives information only about temperature. For this reason, a relationship between temperature and emissive power must be evaluated.In this way,a comparison, between simulation results and real images collected during the experimental campaign, will be possible. Thus, a calibration of the simulated thermal camera in the range $[0 - 600°C]$ is essential. The curve in Figure 4.12 represents a polynomial interpolation, which has the following expression:

$$y = ax^2 + bx + c$$

The errors of the emissive power are caused by the numerical evaluation of the Planckian integral. An error of the 0.5% has been estimated in excess.

The fit parameters are:

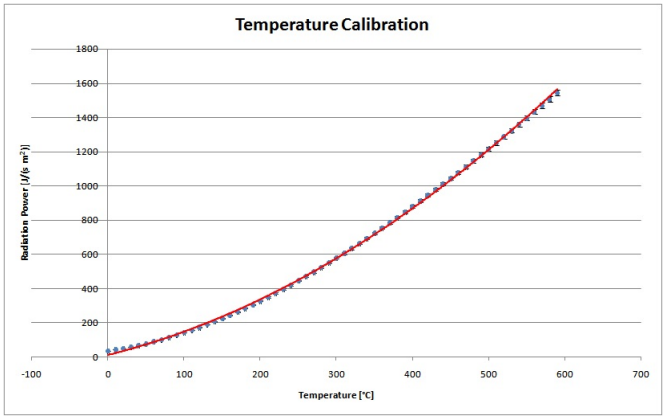

Figure 4.12: Temperature Calibration Fit - J(T)

- $a = (321.8 \pm 1.8) \times 10^{-5} \frac{J}{s\, m^2\, °C^2}$
- $b = (795.4 \pm 6.1) \times 10^{-3} \frac{J}{s\, m^2\, °C}$
- $c = (34.06 \pm 0.25) \frac{J}{s\, m^2}$

4.5 The perspective distortion

The consequences of perspective distortion on the calorimeter vision are analyzed in this section. The description of these geometrical and optical behaviours is important to properly set the parameters of the simulation and to narrowly simulate the phenomena.

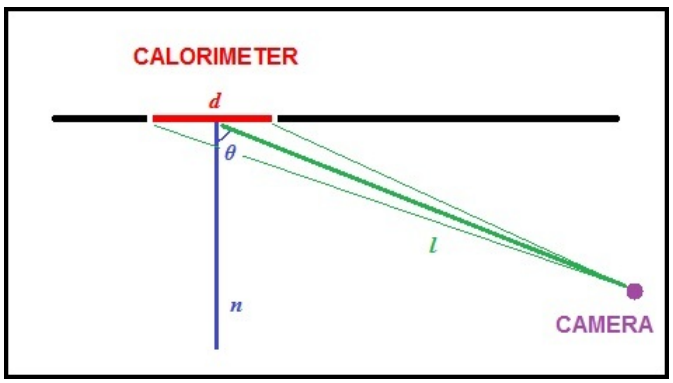

Figure 4.13: Trasversal perspective distortion scheme

When the camera is not frontal with respect to the tile, there is another perspective distortion which has to be included in our dissertation, for replicating the experimental conditions accurately. As can be seen in Figure 4.13, there is a reduction of the trasversal calorimeter dimension that, for the big distances of the camera with respect to tile dimensions, can be approximated with the following trigoniometrical relation.

$$d' = d \sin(\frac{\pi}{2} - \theta)$$

Chapter 5

The simulation results

The results obtained during the simulation campaign are reported in this chapter. At the end of this chapter, it will be analyzed to what extent the moiré pattern can affect the experimental results of STRIKE calorimeter in SPIDER test facility.

5.1 Simulation results

This section contains a description of the results of numerical simulations applied to the calorimeter tile shown in Figure 2.5. The rear side of the tile comprises $2.5mm \times 2.5mm$ prongs surrounded by $0.5mm$ wide trenches. The total dimension of the tile is 100mm x 90mm The distance between thermal camera and calorimeter has been varied. The parameter PIX, which is the parameter that changes in the simulations, is the T-grid cell that thermal camera "sees" on the tile. It can be expected that the image of the tile is well defined when PIX is smaller than the trench size. On the contrary, the image will be affected by moiré aliasing when PIX increases.

5.1.1 Frontal view.

The trasversal view angle is $\theta = 0°$ in the first series of images. The temperature of the prong is $T_{MIN} = 100°C$, while trench temperature is $T_{MAX} = 150°C$. These temperatures have been chosen because $\Delta T = 50°C$ and more will be common in STRIKE experimental condition.

The correct view of the tile is verified only for the smallest value of PIX= $0.1mm$, Figure 5.1a; in this case, the dimension of thermal camera pixel is smaller than trench dimension. In the second image, Figure 5.1b, a worsening of temperature definition can already be noticed. A strong presence of moiré

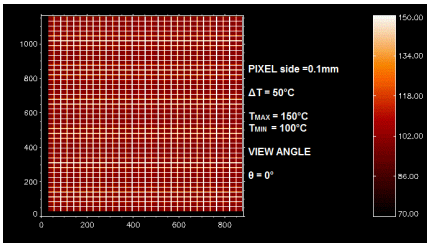

(a) PIX = 0.1mm

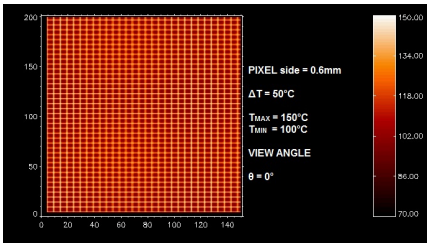

(b) PIX = 0.6mm

Figure 5.1

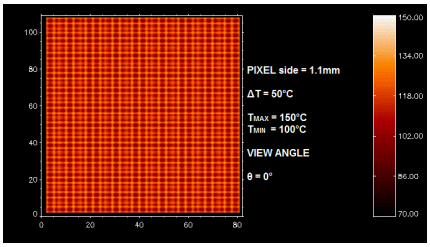

(a) PIX = 1.1mm

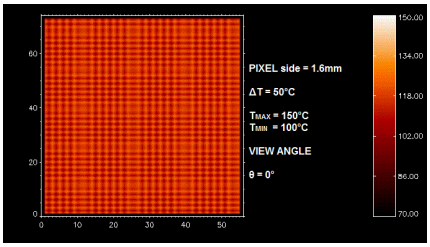

(b) PIX = 1.6mm

Figure 5.2

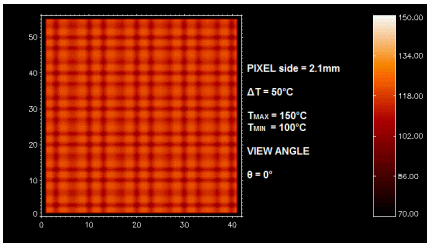

(a) PIX = 2.1mm

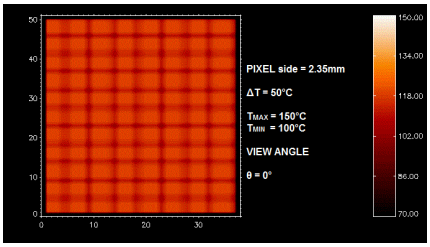

(b) PIX = 2.35mm

Figure 5.3

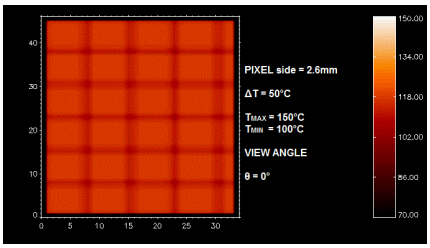

(a) PIX = 2.6mm

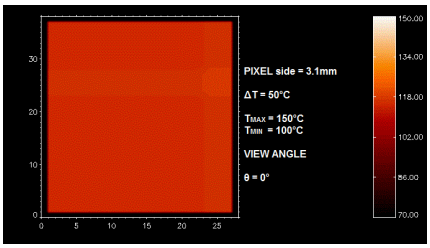

(b) PIX = 3.1mm

Figure 5.4

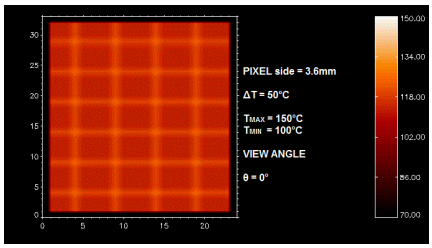

(a) PIX = $3.6mm$

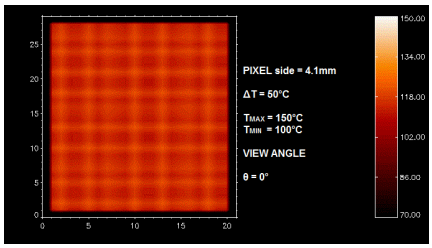

(b) PIX = $4.1mm$

Figure 5.5

patterns affects the other images. This phenomenon can be theoreticaly interpreted as a combination of two parallel moiré patterns, already described in section 3.2. One pattern goes from top to bottom, while the other from left to right. Two interesting simulations are listed in figure 5.2b and 5.4b. In the first case, PIX= $1.55mm$ is about the half of the sum of pin side plus trench; the pattern resulted is a regular "chessboard". This could be confused with the original image, but it is completely distorted for what concerns both trench dimension and values of the maximum and minimum temperatures. In the second image PIX= $3.05mm$, a value equal to the sum of pin side plus trench. In this situation, a monocromatic image occur on the calorimeter surface, with a complete flattening of temperature differences. Another interesting result consists in a sort of parallelism between moiré patterns for PIX bigger and smaller than $3mm$. This effect occurs because when the resonance value of PIX is exceeded, the mutual difference between C-grid and T-grid step has the same values as before the resonance. However, maximum and minimum temperature are inverted. This symmetry can be appreciated by comparing figure 5.4a and 5.5a.

5.1.2 Trasversal view.

The behaviour of moiré patters is analized for various ΔT in the following three simulation series. The information we are interested in for STRIKE data analysis is T_{MIN}, which is the temperature of the prongs. Thus, by studing moiré patterns in different gap temperature conditions is important to understeand if the low temperature is predominant or if the moiré profile is influenced by the highest one. In this last eventuality, the misure of STRIKE would be heavily compromised. The view angle was fixed to 55°; this value has been chosen because it is the same angle used in the LASER test, reported in chapter 2. In this way, a comparison between simulation and experimental results will be possible.

- **SIMULATION 1:** In the first simulation (from Figure 5.6 to 5.9) the trasversal view angle is $\theta = 55°$. The prong temperature is $T_{MIN} = 30°C$, while trench temperature is $T_{MAX} = 50°C$. Thus, $\Delta T = 20°C$.

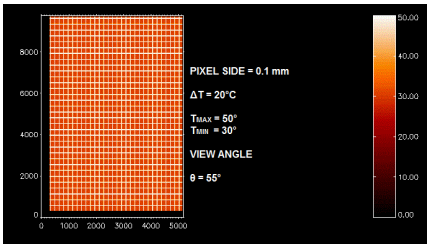

(a) PIX = $0.1mm$

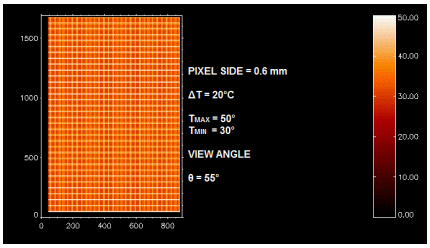

(b) PIX = $0.6mm$

Figure 5.6

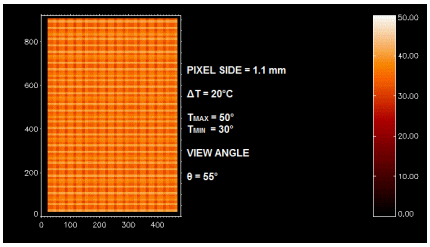

(a) PIX = $1.1mm$

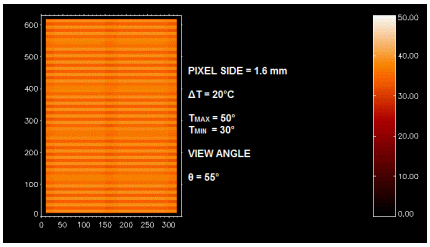

(b) PIX = $1.6mm$

Figure 5.7

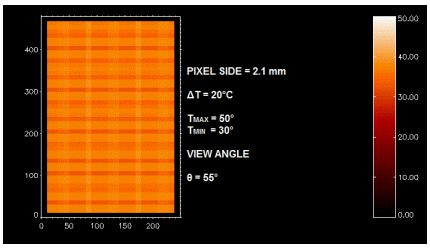

(a) PIX = $2.1mm$

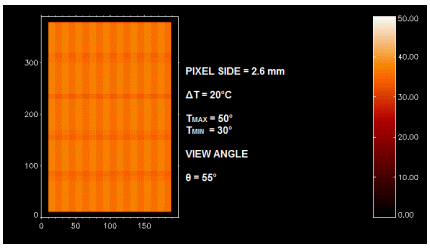

(b) PIX = $2.6mm$

Figure 5.8

- **SIMULATION 2:** In the second simulation (from Figure 5.10 to 5.13) the trasversal view angle is again $\theta = 55°$. The prong temperature is $T_{MIN} = 30°C$, while trench temperature is $T_{MAX} = 70°C$. Thus, $\Delta T = 40°C$.

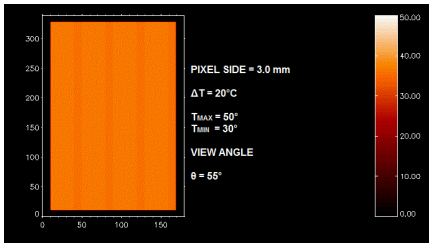

(a) PIX = 3.0mm

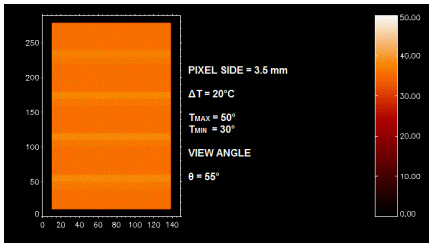

(b) PIX = 3.5mm

Figure 5.9

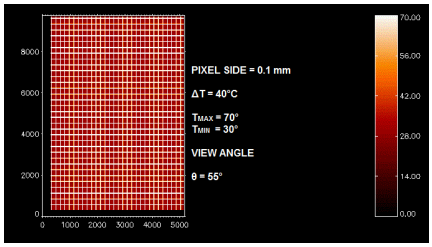

(a) PIX = 0.1mm

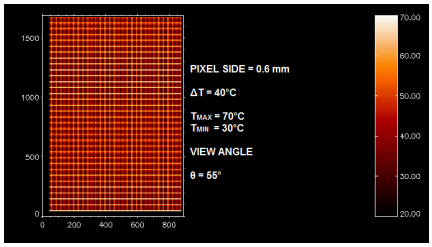

(b) PIX = 0.6mm

Figure 5.10

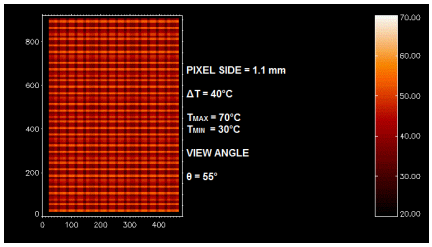

(a) PIX = 1.1mm

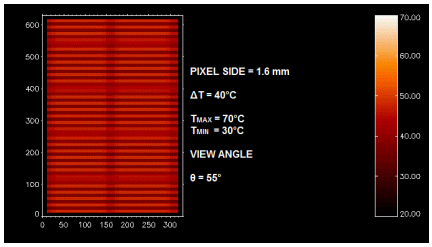

(b) PIX = 1.6mm

Figure 5.11

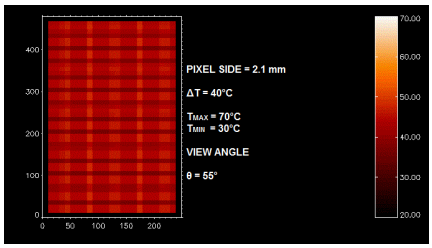

(a) PIX = 2.1mm

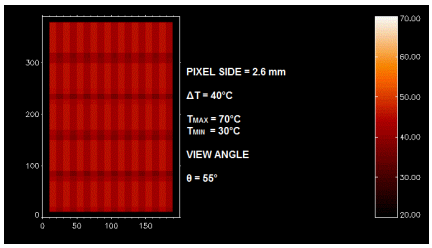

(b) PIX = 2.6mm

Figure 5.12

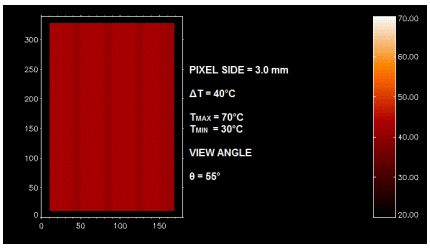

(a) PIX = 3.0mm

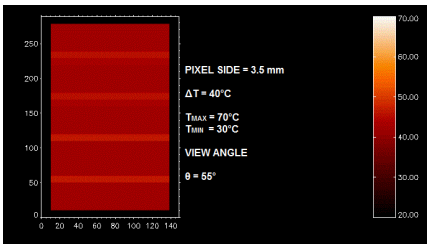

(b) PIX = 3.5mm

Figure 5.13

- **SIMULATION 3:** In the third simulation (from Figure 5.14 to 5.17) the trasversal view angle is again $\theta = 55°$. The prong temperature is $T_{MIN} = 30°C$, while trench temperature is $T_{MAX} = 130°C$. Thus, $\Delta T = 100°C$.

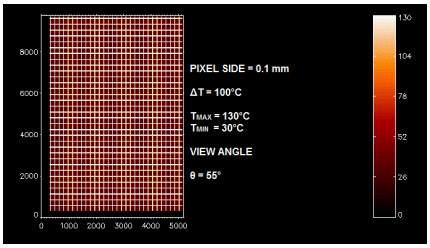

(a) PIX = 0.1mm

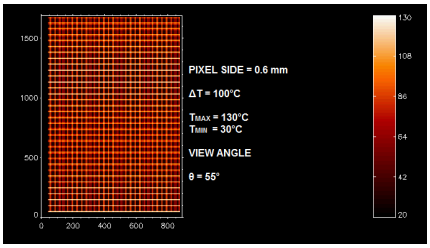

(b) PIX = 0.6mm

Figure 5.14

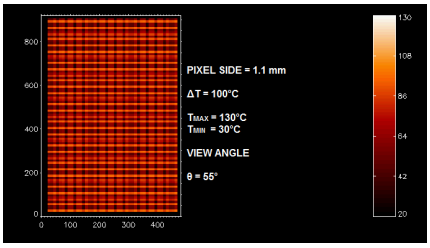

(a) PIX = 1.1mm

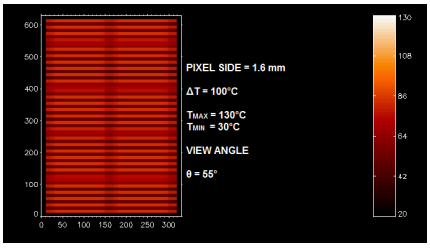

(b) PIX = 1.6mm

Figure 5.15

The first interesting aspect shown by the simulation is that geometrical behaviour of moiré patterns is not influenced by the variation of ΔT. This fact can be appreciated comparing, for example, Figure 5.9, 5.13 and 5.17,

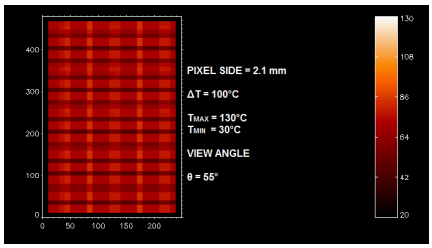

(a) PIX = 2.1mm

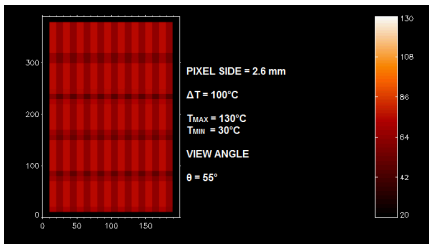

(b) PIX = 2.6mm

Figure 5.16

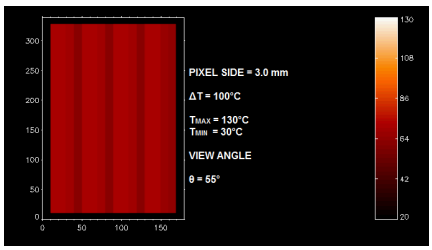

(a) PIX = 3.0mm

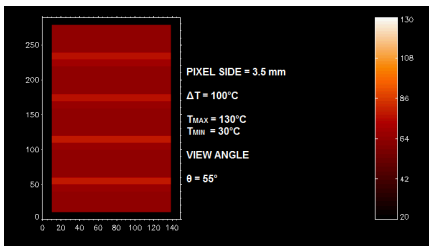

(b) PIX = 3.5mm

Figure 5.17

which have the same PIX= 3.5mm. Even if T change, geometrical pattern is the same. This fact occurs because the geometry of moiré pattern is defined by the geometry of the two overlapping grids and not by their "temperatures", as explained in chapter 3.

Another aspect to underline is that the prong temperature, which is the value we are intersted in, is heavily distorted in the simulation with $\Delta T = 40°C$ and $\Delta T = 100°C$ with respect to the simulation with $\Delta T = 20°C$. This fact could cause a serious problem in STRIKE measures, in particular when the distance between calorimeter and thermal camera is high.

5.1.3 Generic perspective view

The previous simulation have been important to identify the main aspects of the phenomenon, however they do not narrowly reproduce the typical experimental conditions of SPIDER explained in the introduction of this work. In the previous section, it has been supposed that the perspective distortion occurs only for one axis, while the other mantains a frontal view. However, in SPIDER there will be a general perspective distortion. This fact causes the complete loss of orthogonality of C-grid, an example is furnished

in Figure 5.18. A regular variation of the slope has been imposed to construct a realistic reproduction of SPIDER C-grid.

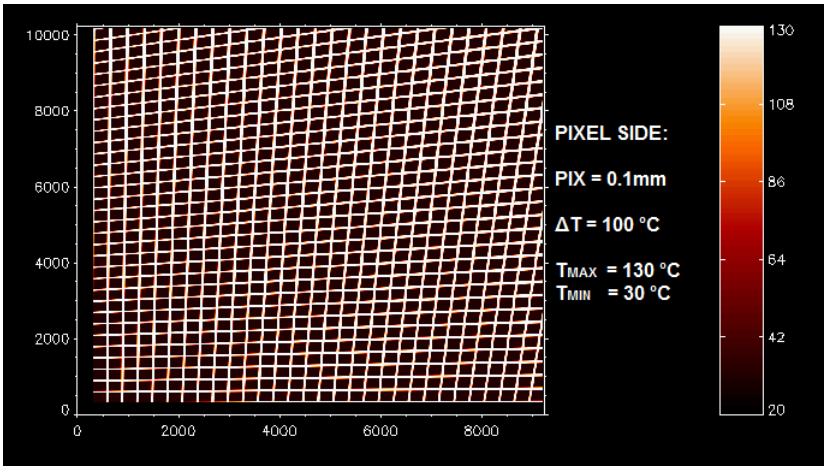

Figure 5.18: General perspective distortion - PIX= $0.1mm$

The presence of curved complex pattern can be immediatly noticed when pixel dimension increases. In the following simulation (Figure from 5.19 to 5.22), the prong temperature is $T_{MIN} = 30°C$, while trench temperature is $T_{MAX} = 130°C$. Thus, $\Delta T = 100°C$.

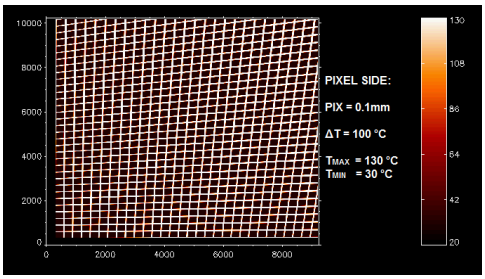

(a) PIX = $0.1mm$

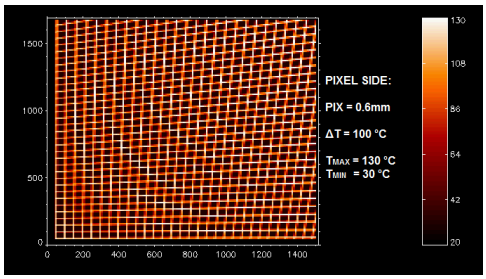

(b) PIX = $0.6mm$

Figure 5.19

5.2 Result analysis

As explained in section 1.4, the typical dimension of pixel side can vary between $1.4mm$ and $2.4mm$ at most. This means that, in order to obtain good measures, temperature values have not to be havily distorted by moiré aliasing, when PIX varies in its characteristic range. The graph listed in Figure

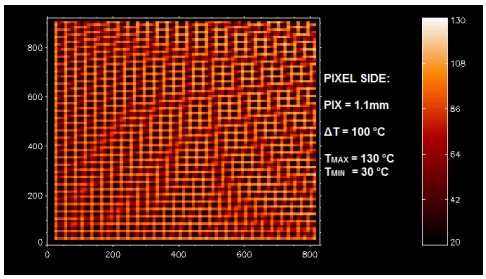

(a) PIX = 1.1mm

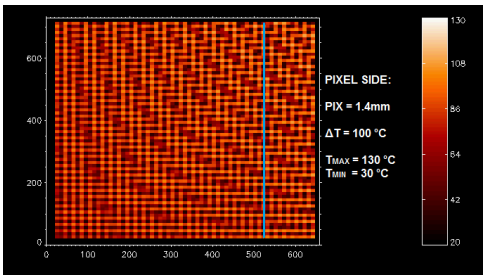

(b) PIX = 1.4mm

Figure 5.20

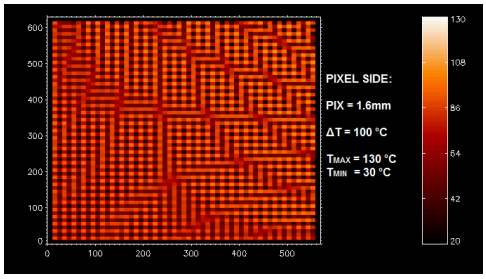

(a) PIX = 1.6mm

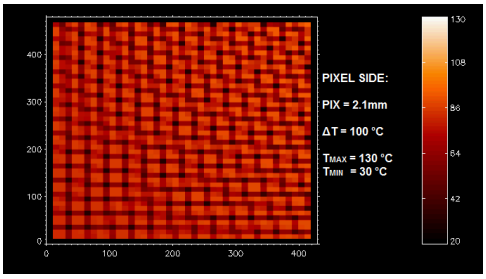

(b) PIX = 2.1mm

Figure 5.21

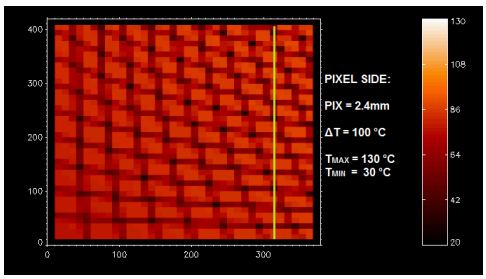

(a) PIX = 2.4mm

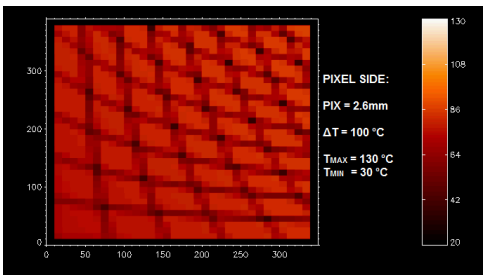

(b) PIX = 2.6mm

Figure 5.22

5.23 helps us to discuss the temperature profile distortion. In this graph, the temperature profile has been plotted as function of a vertical section of the tile, represented in Figure 5.20b.The values of x axis are expressed in pixel. As the graph shows, the information about the temperature of the prongs ($30°C$) is completely lost in most of the graph, when PIX= $1.4mm$. Three peaks occur when the pixels reveal moiré maximums, while the two regions between the peaks correspond to moiré minimums. Only in these last two regions, the original prong temperature can be recognised for very few pixels. Anywhere else, the trench temperature dominates and the profile is completely distorted, with negative consequences for the experimental measures.

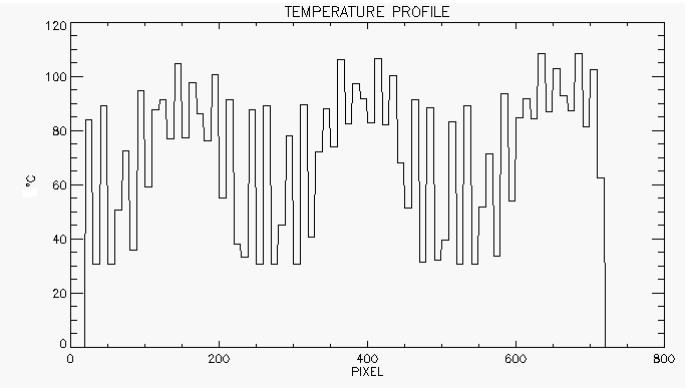

Figure 5.23: Temperature profile of vertical section. PIX= $1.4mm$

The result is totally distorted when PIX= $2.4mm$. The graph in Figure 5.24 shows the temperature profile of a vertical section, when PIX= $2.4mm$. The section is highlighted with a green line in Figure 5.22a. The prong temperature ($30°C$) is never reached and the result is unsuitable for the experimental determination of the temperature profile.

For both graphs just reported, the scale of x axis have been enlarged to better appreciate the rugged trend. Even if the number of pixels has increased, the dimensions of the tile are the same as in the previous simulations ($100mm \times 90mm$).

5.3 Variable temperature profile

In the previous simulations, only tiles with constant prong temperatures have been simulated. However, SPIDER experiment will focus its efforts in measuring the properties of various beamlets, which entails a non-uniform temperature profile on STRIKE surface. For this reason, in the present

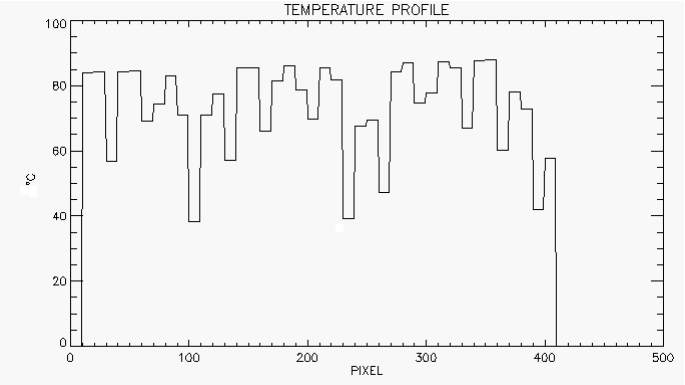

Figure 5.24: Temperature profile of vertical section. PIX= $1.4mm$

section a variable temperature profile is simulated and then, the distortions caused by moiré pattern will be analyzed.

The image of the tile and of the temperature profile used in the simulations is shown in Figure 5.25, with an high definition (PIX= $0.1mm$). The temperature profile of the cental section can be appreciated in the graph reported in Figure 5.26. As in the previous simulations, the trench temperature is higher than prong temperature. The maximum prong temperature is $450°C$ at the center of the beamlet, while the minimum prong temperature is $30°C$ at the tile edges. The trench temperature at the center of the beamlet is $620°C$, while it is $130°C$ at the edges. The temperature values just reported depend on the results of the simulations. A gaussian profile has been used for simulating the beamlet, which has a circular simmetry. $\sigma_x = \sigma_y = 4.2mm$ for our gaussian profile. The Full Width at Half Maximum of the distribution is about ($10mm$). For this first simulations set, a frontal view for the infrared camera has been supposed.

In the following images, the pictures resulted from the simulation are reported at various distances between camera and tile, with the relative temperature profile at the center of the peak. The images have been enlarged on the peak zone; in the rest of the tile, usual moiré patterns occur. However, the same C-grid has been used for all the simulations

The same results as the previous simulations have been obtained with a not uniform temperature profile. The temperatures recorded by the thermal camera are generally greater than the original temperatures, for all values of PIX. To give an example, in Figure 5.27b the temperature at the center of the peak is about $580°C$, while the real temperature of the prongs we are interested in is considerably lower, $450°C$. The distortion due to trench temperature is thus relevant and can invalidate the measures of the beamlet

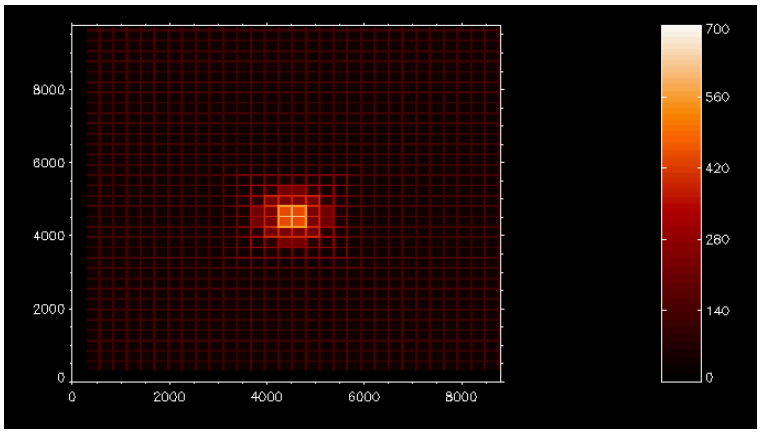

Figure 5.25: Tile with peak. PIX= $0.1mm$

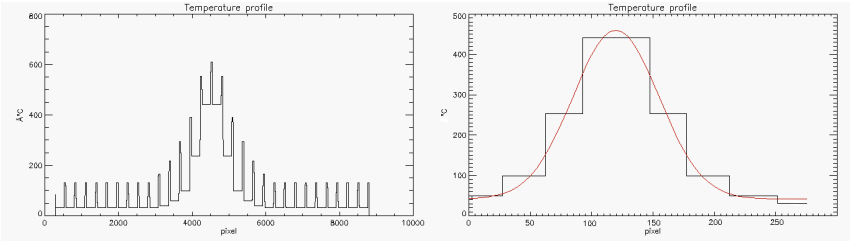

(a) Temperature profile of peak section. PIX= $0.1mm$

(b) Prong Gaussian curve

Figure 5.26

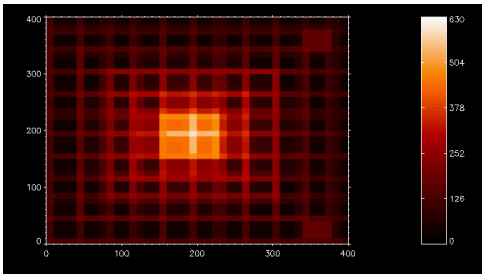

(a) PIX = $0.8mm$

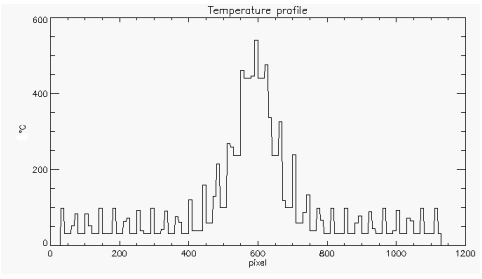

(b) Temperature profile

Figure 5.27

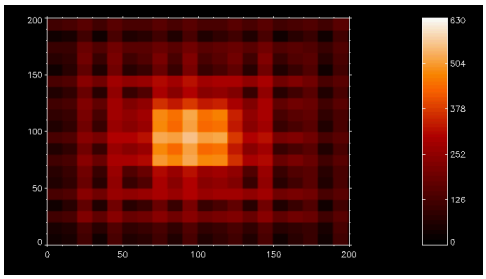

(a) PIX = 1.2mm

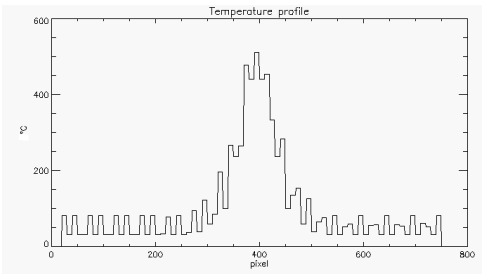

(b) Temperature profile

Figure 5.28

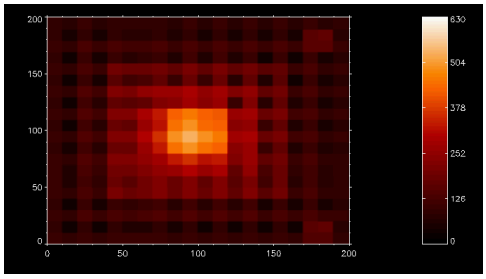

(a) PIX = 1.6mm

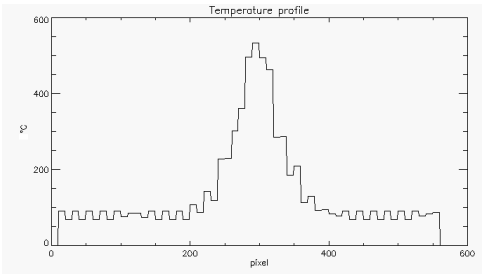

(b) Temperature profile

Figure 5.29

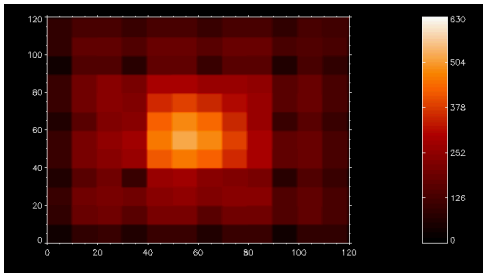

(a) PIX = 2.0mm

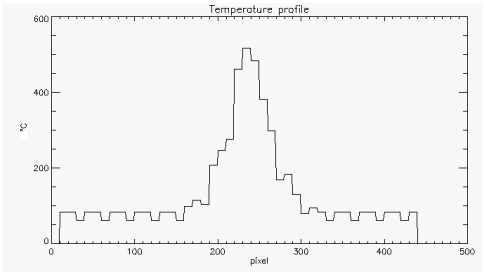

(b) Temperature profile

Figure 5.30

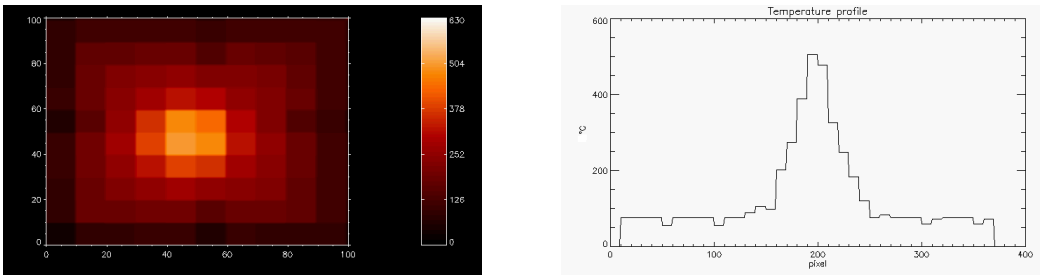

(a) PIX = 2.4mm (b) Temperature profile

Figure 5.31

properties. Another important aspect is that the peaks can become asymmetric beacouse of the presence of moiré pattern which crosses the peak. An example of peak asymmetry can be appreciated in figure 5.30b.

In the following two images (Figure 5.32 and 5.33), the peak is viewed in perspective condition. The moiré pattern can easily be recognised in this simulated situation as well. The temperature of the peak is distorted and obtaining information about the beamlet properties is very difficult.

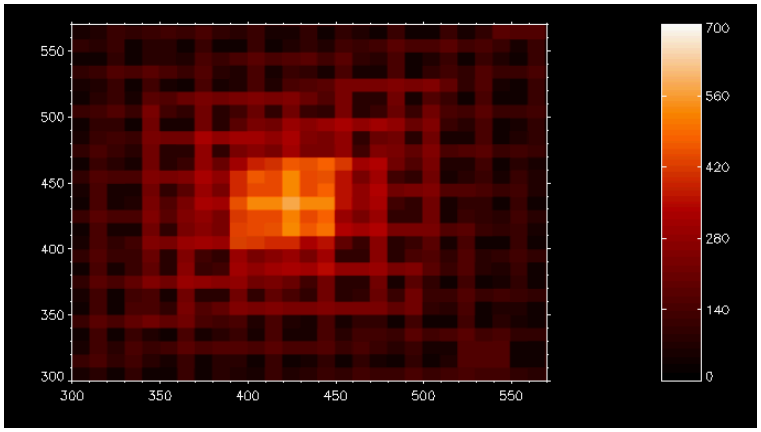

Figure 5.32: Tile with peak - perspective view. PIX= 1.2mm

5.4 Verification of results

The correct operation of the simulation is analyzed in this section. As explained before, moiré effect on the peak is caused by the higher energy flux emitted from the trench zone. If the simulation works correctly, a reduction

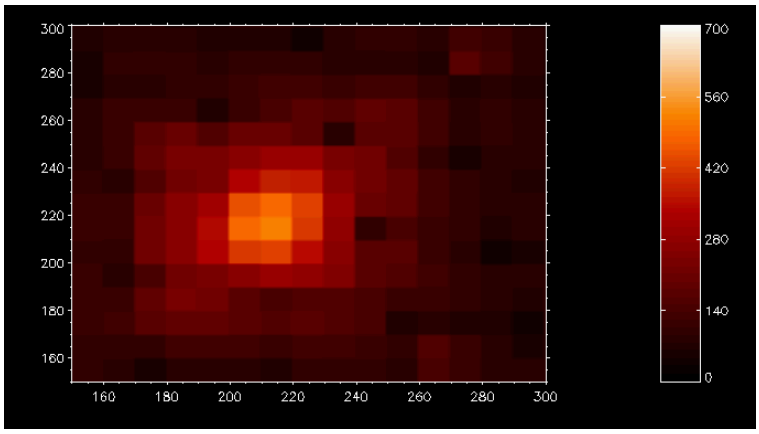

Figure 5.33: Tile with peak - perspective view. PIX= $2.4mm$

of trench dimension will produce a gradual disappearence of the moiré effect. For this reason, Two simulations have been done upon decreasing the dimension of the trench.

The temperature profile is the same as the previous simulations of section 5.3. In the first simulation, the dimensions of prongs are $2.5 \times 2.5mm$, while trench dimension is $0.1mm$.

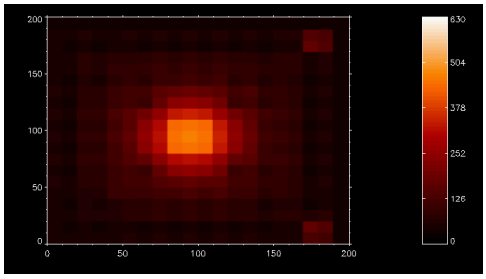

(a) PIX = $1.4mm$

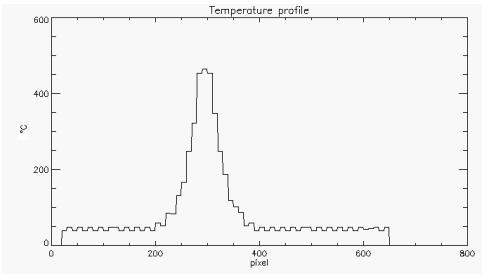

(b) Temperature profile

Figure 5.34

In the second simulation, the dimensions of prongs are $2.5 \times 2.5mm$, while trench dimension is $0.05mm$.

In the first simulation, temperature profile reaches a maximum of about $470°C$. The results are shown in the graphs of Figure 5.34b and 5.35b. This value of temperature is very close to the real temperature of the prongs ($450°C$) and this means that the trench contribution is rather small. When trench dimension is $0.05mm$, the maximum temperature reached is about $450°C$, as can be noted in Figure 5.36b and 5.37b. In this case, the contribution of the trench is totally negligible and the real temperature of prongs

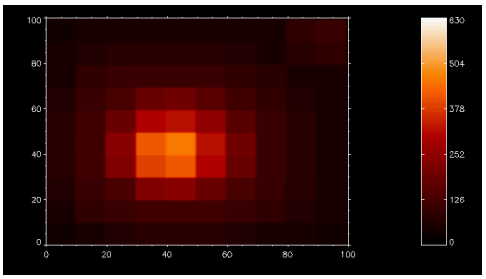

(a) PIX = 2.4mm

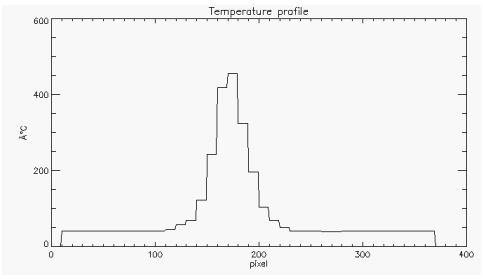

(b) Temperature profile

Figure 5.35

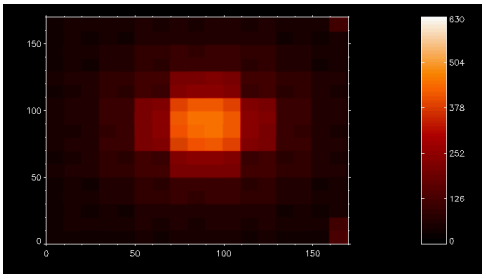

(a) PIX = 1.4mm

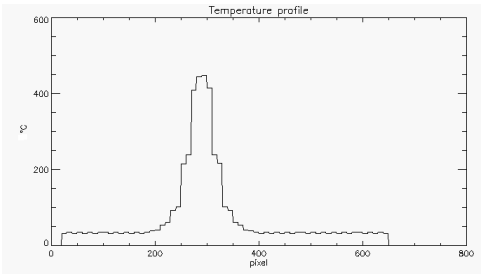

(b) Temperature profile

Figure 5.36

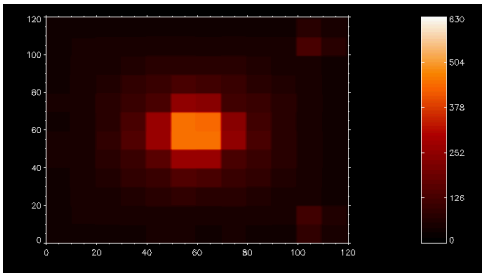

(a) PIX = 1.4mm

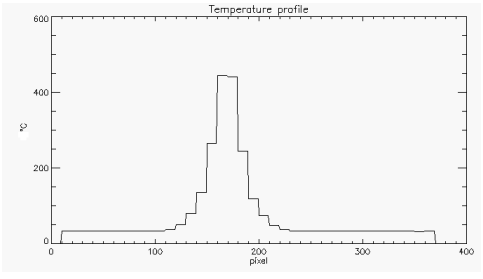

(b) Temperature profile

Figure 5.37

is correctly measured by the thermal camera. The results obtained are thus positive and the simulations operate well. Indeed, it has been demonstrated that when the trench dimension decreases, the moiré effect disappears.

5.5 Alternative geometrical configurations

An alternative geometrical configuration for STRIKE tile can be considered, in order to improve the mechanical and thermal behaviour of the tile. This alternative configuration exhibits the following features in condition of frontal view:

- Prong dimension is $3.0 \times 3.0mm$.
- Trench width is $1.0mm$.

Some simulations using the geometrical properties of this alternative configuration have been done. The main aspect that has been analyzed consists in quantifying the distortion of the peak in condition of generic perspective view. A gaussian profile has been adapted to the temperature profile of the tile by least-squares fitting. The increase of pin and trench dimension causes a loss of the definition of beamlet gaussian profile. A strong perspective view has been imposed and this causes a substantial decrease of trench dimension, while pin dimensions increase. The new geometrical properties after perspective distortion are:

- Prong dimension is $3.8 \times 3.8mm$.
- Trench width is $0.2mm$.

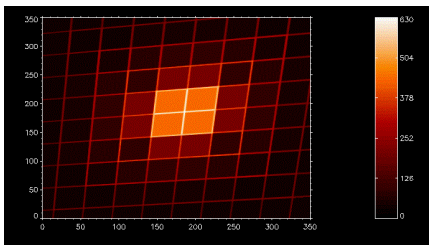

(a) PIX = $0.1mm$

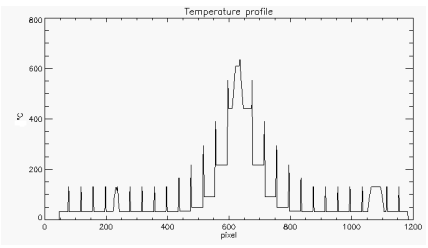

(b) Temperature profile

Figure 5.38

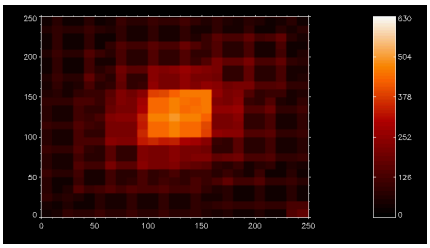

(a) PIX = 1.4mm

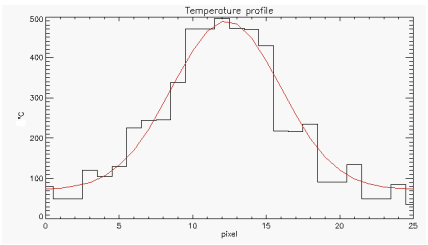

(b) Temperature profile

Figure 5.39

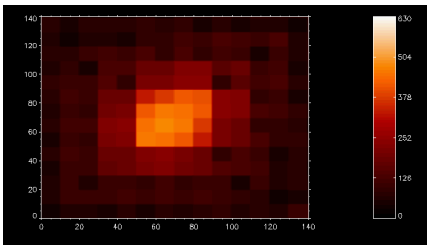

(a) PIX = 2.4mm

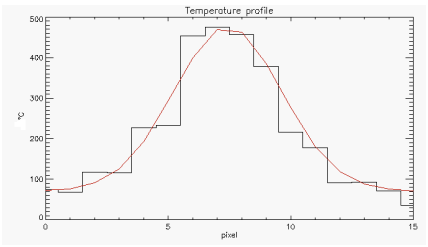

(b) Temperature profile

Figure 5.40

The analytical expression of the gaussian surfaces are:

$$F(x,y) = A_0 + A\, e^{-U/2}$$

$$U = \left(\frac{x-h}{a}\right)^2 + \left(\frac{y-k}{b}\right)^2$$

where the parameters of the function are:

- axis lengths are 2a and 2b, in the X and Y axes, respectively.
- center is at (h, k).
- A_0 is the background temperature.

The temperature profile of the well defined peak (PIX = 0.1mm) is reported in Figure 5.38b; the higher temperature of trench zone can be easily appreciated. Two simulations have been done for PIX= 1.4mm and PIX= 2.4mm, which are the extremes of PIX range. The results are shown in Figure 5.39b and 5.40b. The real number of pixels is reported in the x axis of the temperature profile, while the values in x and y axes of Figure 5.38a and 5.39a are due to a reshaping for better displaying the peaks.

For the first fit (PIX = $1.4mm$):

$$A_0 = 72.4°C\ A = 418.7°C\ a = 3.69pix = 5.2mm\ b = 3.69pix = 5.2mm$$

$$h = 12.30pix = 17.3mm\ k = 12.30pix = 17.3mm$$

For the second fit (PIX = $2.4mm$):

$$A_0 = 70.39°C\ A = 413.32°C\ a = 2.21pix = 5.3mm\ b = 2.21pix = 5.3mm$$

$$h = 7.43pix = 17.8mm\ k = 7.43pix = 17.8mm$$

The parameter errors have been omitted.

The temperature distortion is not as relevant as in the previous simulations, however the increase of temperature values consists in about $30-40°C$. This is a tolerable discrepancy for SPIDER experimental proposals. Another important result consists in quantifying the distortion of the peak. When a high perspective occurs, the peak loses its circular simmetry and it is stretched in the perspective direction. This causes an enlargement of the peak in a particular direction of about $20 - 30\%$, depending on how strong the perspective is.

5.6 Trench contribution in STRIKE experimental condition

In this section the contribution of the trench zone is evaluated in STRIKE experimental conditions. The main proposal is to estimate the limit distance x from the normal under which the bottom of the trench is no more viewed by the termal camera.

As explained in Figure 5.41, this condition occurs when $\theta' \geq \theta''$. By using the trigonometric relations, the following non linear equation can easily be obtained:

$$\arctan \frac{x}{L} = \arctan \frac{x + \delta x}{L + \delta L}$$

The geometrical properties of STRIKE are: $L = 2 - 3m$ approximately, $\delta x = 0.5mm$ and $\delta L = 8mm$. For high value of L with respect to x, the previous equation can be linearized.

$$\frac{x}{L} = \frac{x + \delta x}{L + \delta L}$$

$$\frac{x}{L} = \frac{x}{L + \delta L} + \frac{\delta x}{L + \delta L}$$

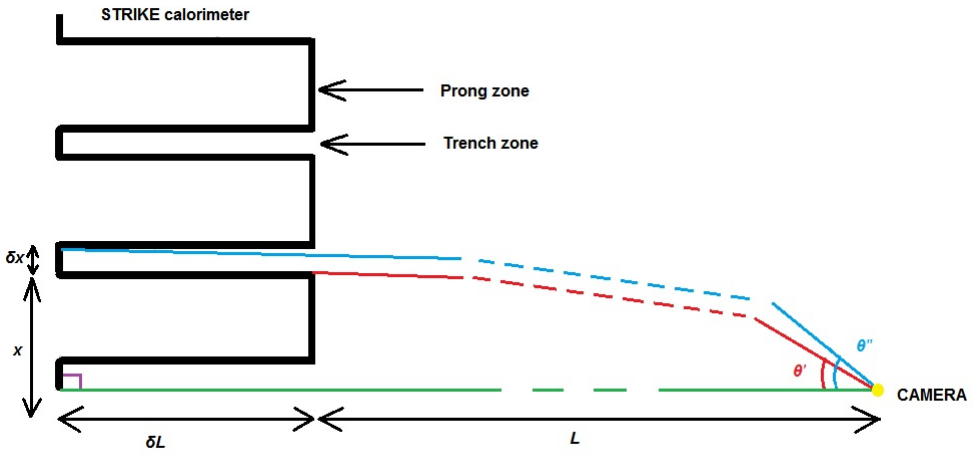

Figure 5.41: STRIKE calorimeter and thermal camera scheme.

$$x\left(\frac{1}{L}-\frac{1}{L+\delta L}\right)=\frac{\delta x}{L+\delta L}$$

$$x=L\frac{\delta x}{\delta L}$$

When, for example, $L=3m$, $x=5\times10^{-4}\frac{3}{8\times10^{-3}}=18.75cm$. The result shows that in the horizontal direction the measurements of the thermal camera viewing a castellated tile will be affected by the bottom of the trench over a distance of a beamlet group; in the vertical direction, the viewing angle is anyway such that the camera will not see the bottom of the trench (see figure 1.6).

To summarize, in the thermal images of STRIKE the vertical trenches will create a combination of the results of section 5.3 and 5.4, depending on the location; the horizontal trenches on the other hand will always be treated as in section 5.4.

Chapter 6

Comparison with real images

The main proposal of this chapter is to compare the results of the simulations with the images provided by tests with LASER, already described in section 2.3. In this way, the correctness of the initial supposition about the moiré effect can be confirmed and it will be proven that the patterns on the tile are really caused by moiré phenomenon. The experimental conditions of the two LASER tests where moiré patterns are observed are:

- **TEST 1:** Distance between camera and tile $d_1 = 2.9m$. View angle with respect to the tile normal $\theta_1 = 55°$.
- **TEST 2:** Distance between camera and tile $d_2 = 3.38m$. View angle with respect to the tile normal $\theta_2 = 55°$.

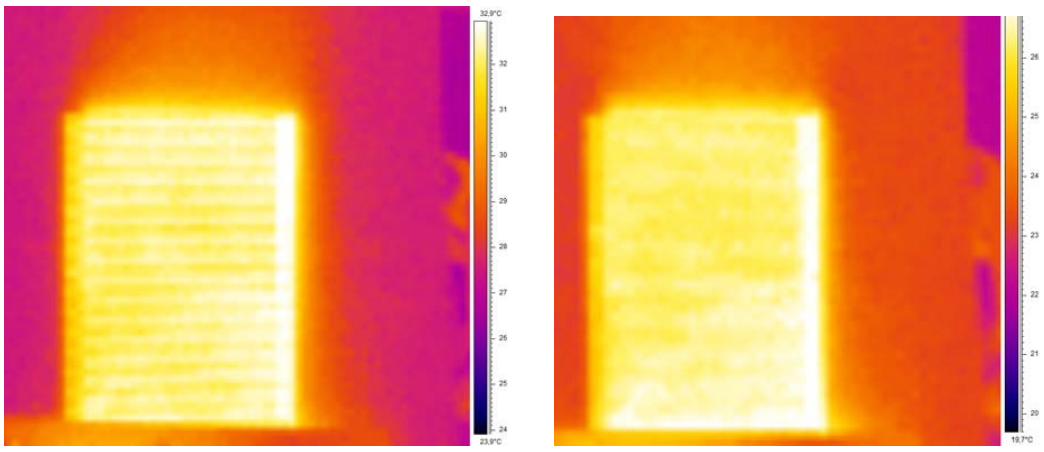

(a) TEST 1 (b) TEST 2

Figure 6.1

The thermal camera images of the two tests are reported in Figure 6.1a and 6.1b. The typical band pattern can be easily recognised. If the supposition about moiré phenomenon is correct, the same band structure as the original images will occur in the simulations.

6.1 Simulation of the two test

The real temperatures (prong and trench) of the first test have been obtained from a well defined image of the tile reported in Figure 6.2. In the previous image, the distance between thermal camera and the tile is $0.4m$. $T_{MIN} = 30°C$ for the prong, while $T_{MAX} = 36°C$ for the trench. Obtaining exactly the real temperatures of trench and prong zones is not easy, because the well defined image was produced during a different LASER pulse. Obviously, the starting temperatures of the tile could vary for different pulses. In any case our purposes do not require a high precision and a $\Delta T = 5 - 6°C$ seems thus reasonable. The dimension of the prongs is, as usual, $2.5 \times 2.5mm$ and trench dimension is $0.5mm$. The total dimension of the tile is $100 \times 90mm$. The dimension of pixel side (PIX) must be determined from the two values of d. The two PIX values estimated are $PIX_1 = 2.0mm$ and $PIX_2 = 2.4mm$.

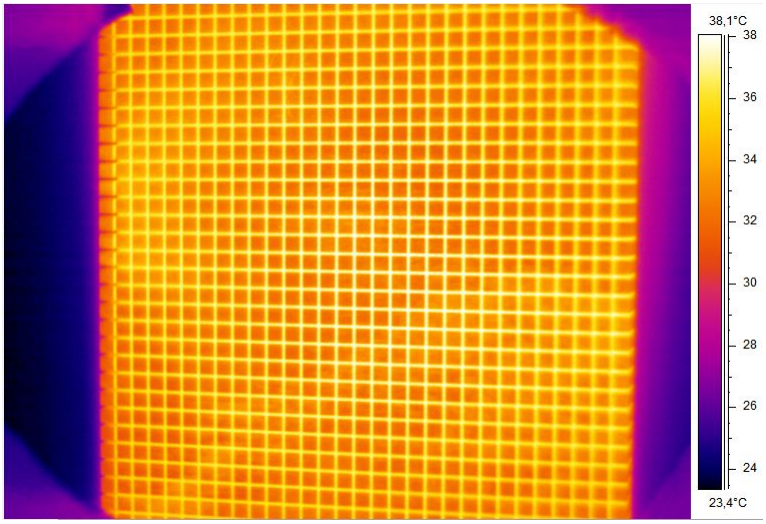

Figure 6.2: Well defined image.

6.1.1 Simulation of Test 1

The result of the first simulation is reported in Figure 6.3. As can be noticed by comparing the simulated tile (Figure 6.3) with the original one (Figure

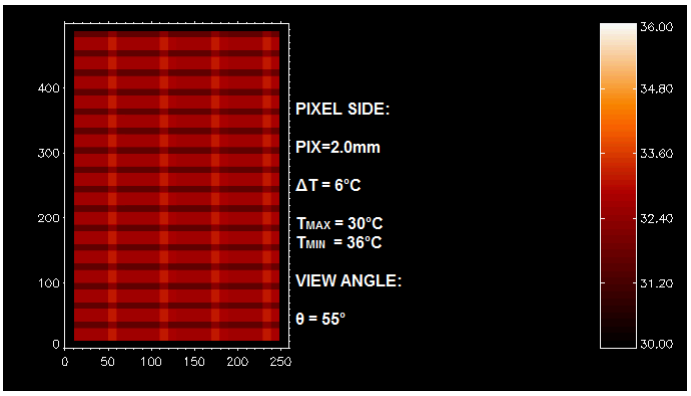

Figure 6.3: Simulation 1. PIX= $2.0mm$

6.1a), the result is very good and the simulated image reproduce the original very well. A temperature profile of a section of the simulated tile has been plotted in Figure 6.4. When comparing the simulated profile with the experimental one, displayed in Figure 6.5, the same number of temperature minimums can be easily recognised.

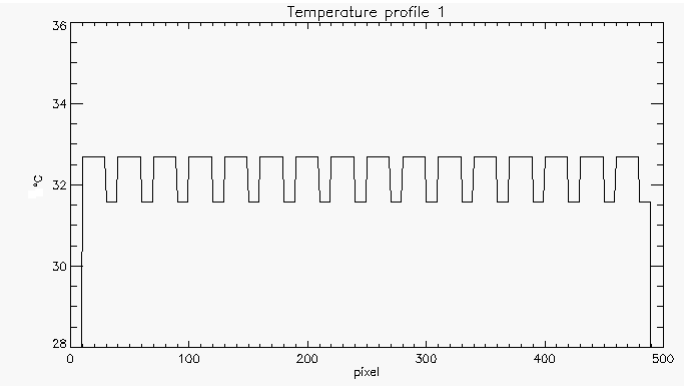

Figure 6.4: Simulated profile - $d = 2.9m$

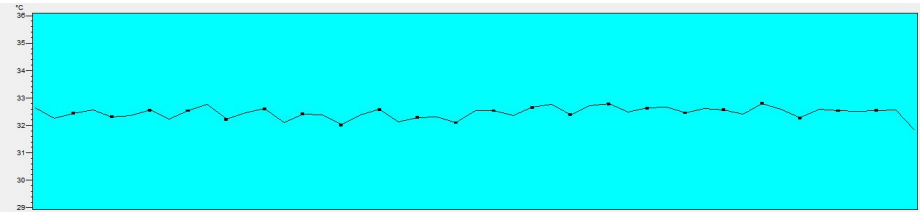

Figure 6.5: Real profile - $d = 2.9m$

6.1.2 Simulation of Test 2

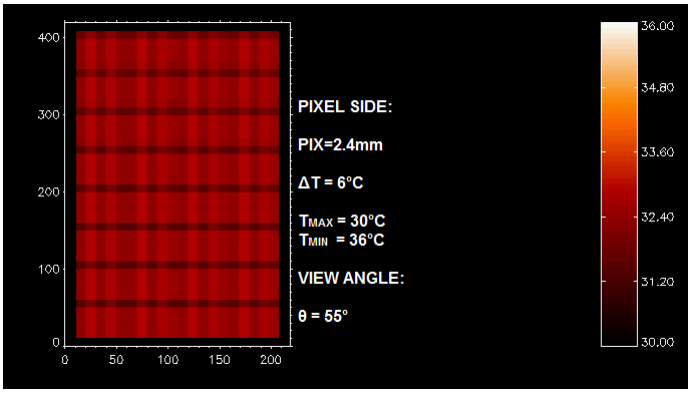

Figure 6.6: Simulation 2. PIX= $2.4mm$

The result of the second simulation is reported in Figure 6.6.The second test is more difficoult to comment, indeed the original image in (Figure 6.1b) is not properly defined. By comparing the original and the simulated images the same number of bands can be recognised. The temperature profile of a section of the simulated tile has been plotted in Figure 6.7. It can be seen that the gap between the highest and the lowest temperature is reduced with respect to the simulation of the first test, as expected from the results obtained in the previous chapter.

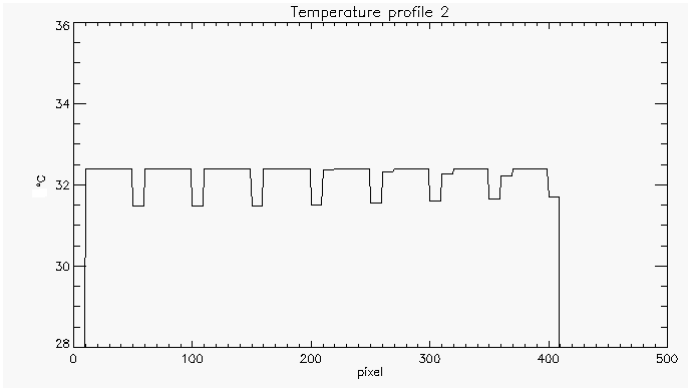

Figure 6.7: Simulated profile - $d = 3.38m$

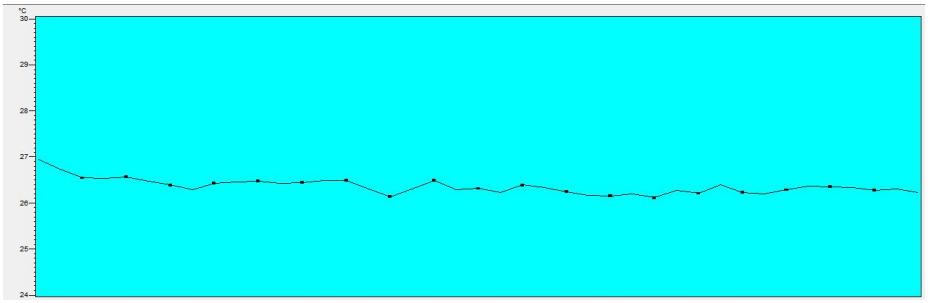

Figure 6.8: Real profile - $d = 3.38m$

6.2 Final considerations

Finally, the results obtained in the simulation are similar to the images provided by the thermal camera. Both the geometry of the pattern and the temperature profile are well reproduced, in particular for what concerns the first test. Indeed, as shown is the previous section, the temperature profile of the second thermal camera image (Figure 6.8) is unfortunately too poorly resolved to provide a quantitative comparation with the simulated image, mainly for what concerns the temperature values. However, a qualitative analysis between real and simulated image shows that the geometry of moiré pattern is well reproduced in our simulation; indeed, also in this case, the same number of bands can be recognised. Probably, the increase of the ΔT could help to have a clearer and univocal comprehension of the results and it could allow an easier comparison. In any case, the band patterns revealed by the camera can be attributed to the moiré effect and it can be established that the simulations replicate the experimental results with a good precision.

Chapter 7

Conclusions

ITER is an international project whose aim is to verify the technological feasibility of a nuclear fusion reactor, confining a plasma within a Tokamak configuration. To increase the temperature of the plasma, two injectors of high energy neutral particles will be employed. In Padua, two test facilities are being built to study the properties of the neutral source and the neutral beam. SPIDER, which is the name of one of the two test facilities, will accelerate a $40A$ negative hydrogen or deuterium beam to $100keV$.

STRIKE is one of the diagnostic elements of SPIDER and consists in a calorimeter made of 16 graphite tile, which might be made anisotropic with a suitable manufacturing consisting in digging deep trenches in a graphite tile. However, this manufacturing causes an uneven temperature distribution on the rear side of STRIKE, which produces a particular spatial aliasing phenomenon in the thermal camera images, when the distances between the two devices are high enough, so that the area viewed by a pixel of the thermal camera is comparable to the distance between the trenches in the tile surface. This effect can be attributed to the so called moiré effect, which arises when two different grids are superimposed. The evidences of this behaviour have been obtained in some LASER tests on a tile prototype. In this work, after analyzing the theory of moiré effect, I tryed to reproduce the experimental phenomenon writing an IDL code. The program simulates the emissivity of the rear side of the tile and the operating principle of the infrared camera, in various conditions.

The first question I tried to answer, is whether the observed pattern could be attributed to moiré phenomenon. The results obtained from the simulations have been compared to the images produced by the thermal camera and a good correspondence between theoretical and experimental data has been confirmed. For this reason the geometrical patterns occurring on the rear side of the tile can be attributed to moiré effect. The second main question

this work addresses is if moiré effect could heavily compromise the measurement process in STRIKE experimental condition, where the distances between calorimeter and thermal camera are high $(2-3m)$. On the one hand, the simulation results reveal that the measure of the beamlet properties is strongly compromised by the patterns which occur on the tile surface. It has been observed that the temperature can result easily distorted by about $50-100°C$. At the same time, the beamlet symmety can be compromised by the pattern presence aswell. On the other hand, the strong presence of perspective distortion can help to reduce the moiré phenomenon, because this produces a reduction of the trench zone seen by the thermal camera. This was simulated as an enlargement of prong dimension. However, the perspective distortion can cause a loss of the circular symmetry of the beamlet and thus a relative elongation.

The results provided in this work, shows that the key point is the dimension of trench zone. Indeed, when the thermal camera "sees" the bottom of the trench, which is the hottest zone, the latter can strongly influence the temperature profile and compromise STRIKE measures. On the contrary, when a relevant perspective distortion occurs and thus the trench bottom is not seen by the camera, the temperature profile is not compromised and the measures are good. In any case, it has been demonstrated that in several expected STRIKE experimental conditions the thermal camera does not see the bottom of the trench but only the sides of the prongs. This means that the measurements of the peak properties should not be too influenced by moiré effect and thus, the thermal camera should see a temperature profile affected by slight distortions.

7.1 Future developments

There are different solutions to improve the system and to avoid the moiré effect. The first option is changing the lens of the camera and enlarging a reduced area of the tile. In this way the resolution of the camera will increase and the real temperature of the prongs can be recognised. This first solution allows to measure the beamlet properties with a high precision, but would require a large number of thermal cameras resulting in an increase of the cost of STRIKE. The second option is using a thermal camera with a bigger sensor. However, this solution could be much more expensive in this case as well. It is cheaper and simpler to revise the design of the system by taking the present results into account, e.g. by slightly rotating the panels with respect to the camera observation direction so that the bottom of the trenches are not directly visible.

The future developments of this work can be resumed in the following three points. Firstly, the distance between the thermal camera and STRIKE calorimeter must be optimized: the real variation of the perspective along the panels supporting the STRIKE tiles must be simulated in detail. Secondly, the spatial resolution which is possible to obtain at such distances have to be experimentally verified. Finally, the present work shows that, from the diagnostic point of view, the graphite option is qualified as an alternative solution to CFC tiles, but the essential condition is a very good strength to mechanical stresses: these studies are currently underway.

Bibliography

[1] M. Kikuchi, K. Lackner, M.Q. Tran, eds. *Fusion Physics*, IAEA International Atomic Energy Agency, (2012).

[2] P. Sonato, V. Antoni et al., *Status of PRIMA, the test facility for ITER neutral beam injectors*,AIP Conference Proceedings 1515, 549, (2013).

[3] P. Agostinetti et al., *Physics and engineering design of the accelerator and electron dump for SPIDER*, Nuclear Fusion 51, 063004, (2011).

[4] P. Franzen et al., *Commissioning and First Results of the ITER-Relevant Negative Ion Beam Test Facility ELISE*, AIP Conf. Proc. 1097, 451 (2009).

[5] U. Fantz et al., *Physical performance analysis and progress of the development of the negative ion RF source for the ITER NBI system*, Nuclear Fusion 49, 125007 (2009).

[6] M. M. Bacal et al. *Basic processes of negative hydrogen ion production and destruction in sources and beams*, Rev. Sci. Instrum. 46.6, (1996).

[7] R. Pasqualotto, *STRIKE thermography. Technical specifications*, RFX_SPIDER_TN_109_r1, (2011).

[8] A. Rizzolo, M. Dalla Palma, M. De Muri, G. Serianni, *Design and analyses of a one-dimensional CFC calorimeter for SPIDER beam characterisation*,Fusion Engineering and Design 85, 2268–2273, (2010).

[9] M. De Muri, G. Serianni, D. Fasolo, R. Pasqualotto, *Assessment of a graphite option for STRIKE tiles*, RFX_SPIDER_TN_324, (2014).

[10] P. Sonato et al., *The ITER full size plasma source device design*, Fusion Engineering and Design 84, (2009).

[11] *Technical Data FLIR SC655 15°*, Flir Sistems, Inc, (2011).

[12] I. Amidor, *The Theory of the Moiré Phenomenon. Volume I: Periodic Layers. Second Editon*, Springer, (2009).

[13] I. Amidor, *The Theory of the Moiré Phenomenon. Volume II: Aperiodic Layers*, Springer, (2007).

[14] C. Cohen-Tannoudji, B. Diu, F. Laloe, *Quantum Mechanics*, Wiley-Vch, (1991).

[15] URL: http://www.exelisvis.com/docs/using_idl_home.html, *Exelis VIS product documentation center.*

[16] E. E. Salpeter. *Nuclear Reactions in the Stars. I. Proton-Proton Chain*, Phys.Rev. 88 pp. 547–553, (1952).